

UNIVERSITY OF MANITOBA

An analysis of the piezoresistive
response of n-type, bottom-up,
functionalized silicon microwires

by

Megan Margaret McClarty

A Thesis submitted to the Faculty of Graduate Studies of The University
of Manitoba in partial fulfillment of the degree of
MASTER OF SCIENCE

in the

Faculty of Engineering

Department of Electrical and Computer Engineering

Copyright ©2014 by Megan McClarty

UNIVERSITY OF MANITOBA

Abstract

Faculty of Engineering
Department of Electrical and Computer Engineering

MASTER OF SCIENCE

by Megan Margaret McClarty

As the world's population increases, the demand for energy also grows. The strain on our limited resources of fossil fuels is unsustainable in the long term. An alternative, renewable method of energy generation must be implemented. Solar energy has good potential as an environmentally sound, unlimited energy source, but solar devices are not yet able to efficiently store energy for later use. A device has been proposed which uses direct sunlight to split water into hydrogen and oxygen. The hydrogen can then be harvested and stored as fuel, solving the question of how to effectively store energy generated during times of peak sunlight for use when sunlight levels are low. The prototype device incorporates arrays of doped silicon microwires which function as light absorbers and current-carriers, driving the chemical reactions that evolve hydrogen from water. This work aims to quantify and characterize the reduction in microwire resistivity that is achievable through application of silicon's piezoresistive properties. Silicon displays a change in electrical resistance as a function of applied mechanical strain. This electromechanical effect has been studied extensively in bulk and top-down (etched) microstructures, but studies on microstructures grown bottom-up have been limited. A simple method is presented for piezoresistive characterization of individual, released, bottom-up silicon microwires. It is shown that these n-type microwires display a consistent negative piezoresistive response which increases in magnitude with increasing doping concentration. It was found that harnessing the piezoresistive response of moderately-doped ($\sim 10^{17} \text{ cm}^{-3}$) n-type wires allowed for a maximum observed reduction in resistivity of 49%, which translated to a 1% reduction in overall system resistance of a prototype unit cell of the artificial photosynthesis device, if all other components therein remained unchanged.

Acknowledgements

I would like to express my appreciation to the school and the Department of Electrical and Computer Engineering for their support and funding via the University of Manitoba Graduate Fellowship. I am also indebted to my supervisors, Drs. Derek Oliver and Michael Freund, for tireless support and inspiration, as well as countless hours of review, encouragement and critique. I could not have finished this degree without the support of my peers and colleagues, namely Jared Bruce, Mike McDonald, Pat Giesbrecht, Sean Ryman, Ankit Gupta, Mahdi Nadimi and Mathias Pielahn. I would also like to thank my parents, family and Garrett Ward, who talked me down when frustrations were high and gave me all the support I could have wished for. And to my faithful horse Justinian, who patiently endured many hours of solid state theorizing without a word of complaint...

To my parents

Contents

Abstract	i
Acknowledgements	ii
List of Tables	vi
List of Figures	vii
List of Copyright Material for which Permission was Obtained	x
Abbreviations	xi
Physical Constants	xii
1 Introduction	1
1.1 Motivation	1
1.1.1 Solar Energy	1
1.1.2 Hydrogen Fuel	3
1.1.3 Artificial Photosynthesis	4
1.2 Thesis Outline	10
2 Background Theory	12
2.1 Piezoresistivity of Silicon	12
2.1.1 Young’s Modulus	15
2.1.2 Strain in a Crystalline Lattice	16
2.1.3 Doped Silicon	20
2.1.4 Strained n-Si	23
2.2 Direct Ohmic Contact to Silicon	28
2.3 Mechanical Strain Model	29
2.4 Doping Concentration Effects	33

2.5	Scaling and Growth Effects	34
2.6	Surface Functionalization	36
2.7	Hypothesis	37
3	Method	38
3.1	Sample Preparation	38
3.2	Electrical Testing	41
3.2.1	Making Ohmic Contact	43
3.2.2	Determining Doping Concentration	47
3.2.3	Effect of Probe Oxidation on Quality of Probe-Silicon Contact . .	49
3.2.4	Effect of Illumination	51
3.3	Strain Application	53
3.3.1	Ex-Situ Quantitative Analysis	54
4	Results and Discussion	55
4.1	n-Si Microwires	55
4.1.1	Set A	55
4.1.2	Set B	57
4.1.3	Set C	60
4.1.4	Comparison	61
4.2	Implications for the Solar Device	65
5	Conclusion	68
A	Appendix	71
	References	73

List of Tables

3.1	Resistance values for uniformly-separated tungsten probes on silver contacts sputtered on an FTO plate prior to etching with KOH, five minutes after etching, and one day after etching.	50
4.1	Experimentally determined gauge factors for Set A.	57
4.2	Experimentally determined gauge factors for thienyl-terminated, non-backfilled microwires with a doping concentration of $(3.6\pm 0.1)\times 10^{17} \text{ cm}^{-3}$ (Set B).	60
4.3	Experimentally determined gauge factors for thienyl-terminated, non-backfilled microwires with a doping concentration of $(6.8\pm 0.8)\times 10^{20} \text{ cm}^{-3}$	60
4.4	Experimentally determined PR coefficient results for all sets	62
4.5	Experimentally determined resistances for n-type wire/polymer prototype system.	66
4.6	Feasible and maximum achieved reductions in resistivity for all three sets.	66

List of Figures

1.1	Photosynthesis is the natural process by which plants convert light energy, water, and carbon dioxide into the carbohydrate sugars required to drive their growth and function. Oxygen is a waste product of this process. The proposed device aims to mimic this process.	5
1.2	The proposed artificial photosynthesis device will be comprised of two arrays of silicon microwires embedded in a proton-permeable membrane. On the anode side (n-type), O ₂ will be evolved; on the cathode side (p-type), H ₂ will be evolved and captured.	5
1.3	Overall system resistance of a unit cell of the microwire/polymer/microwire system. Reducing the resistance of any of the components will help to reduce voltage drop across the system and increase efficiency.	9
2.1	Geometric deformation of a cylinder under an applied force.	13
2.2	The diamond cubic lattice form of single-crystalline silicon.	16
2.3	The Kronig-Penney model represents a one-dimensional crystal lattice as a periodic array of potential wells, where a is the interatomic spacing and b the barrier width.	17
2.4	An example dispersion relation for the Kronig-Penny model in a silicon lattice with original, undeformed interatomic spacing 5Å, continuous across allowed and forbidden energies. Shortening the interatomic spacing a will increase the bandgap; lengthening it will decrease the bandgap. This is illustrated here as $\Delta E_3 < \Delta E_1 < \Delta E_2$, where ΔE_3 corresponds to 15% increase in a and ΔE_2 to a 15% decrease. These strain values are extreme and are used for the purpose of illustration only. Figure plotted in MATLAB.	19
2.5	The Fermi level at absolute zero in a metal. All occupied states exist below the Fermi level at this temperature.	22
2.6	The Fermi level at 0K in a semiconductor, located in the forbidden region between valence and conduction bands.	22
2.7	Band diagram for n-type doped silicon showing the Fermi level of intrinsic silicon (E_{Fi}) and the shift in the Fermi level (to E_{Fn}) resulting from the addition of dopant impurities to the intrinsic silicon. This causes a surplus of electrons in the conduction band in comparison to holes in the valence band ($N_{e-} > N_{h+}$), which shifts the Fermi level of the material.	23

2.8	A shift in the ratio of heavy to light carriers occurs when the lattice undergoes compressive strain. Compressive strain along the y axis induces a transfer of electrons from the transverse valleys to the longitudinal valleys, increasing the proportion of heavy carriers in the y-direction and therefore reducing mobility and conductivity. The solid ellipses indicate the original form of the valleys; the dashed ellipses, the valleys under strain X	26
2.9	The effect of increasing compressive strain on the valley structure of silicon. When no strain ($X = 0$) is applied, the proportion of heavy and light carriers is equivalent. As compressive strain is increased ($X < 0$), a charge transfer increases the proportion of heavy carriers oriented longitudinally with respect to the strain. This increases resistance until the point of saturation ($X \ll 0$). Copyright 2014 by the Cambridge University Press. Used with permission.	27
2.10	Geometric illustration of element of bent wire, where r_c is the radius of curvature, θ the angle, and z the distance between the neutral axis and the point of measurement.	29
2.11	Scaled measurement parameters on microwire under applied stress.	31
3.1	Silicon microwires grown by VLS chemical vapour deposition. Inset scale bar $10\mu\text{m}$. Used with permission. Copyright 2007, AIP Publishing LLC.	39
3.2	Silicon microwires deposited on a glass slide. Lengths varied due to position on growth substrate as well as breakage during removal procedure.	41
3.3	Tungsten (W) probes brought into direct contact with a single silicon microwire.	42
3.4	Electrical circuit formed by tungsten probe - silicon wire - tungsten probe system.	43
3.5	Applied pressure as a function of incremental turns of the probe holder control dial. The horizontal line represents the threshold of $11\text{ mN}/\mu\text{m}^2$ which is required to make direct ohmic contact to single crystalline silicon.	45
3.6	Current-voltage curves for incremental downward turns of the probe control dial, showing strong ohmic behaviour after $1/4$ turn.	46
3.7	The separation distance d_n between the two active tungsten probes was decreased in intervals, with a resistance measurement performed at each stop, for n intervals along the length of a microwire.	48
3.8	Resistance versus separation distance for the first sample, indicating a doping concentration of $(1.7\pm 0.1)\times 10^{17}\text{ cm}^{-3}$	49
3.9	Resistance versus separation distance for the second sample, indicating a doping concentration of $(3.6\pm 0.1)\times 10^{17}\text{ cm}^{-3}$	49
3.10	Current-voltage curves for tungsten W probes on FTO substrate prior to etching with KOH, immediately after etching, and a day after etching.	51
3.11	The effect on current response of silicon microwires under illumination (light on) and in darkness (light off).	52

3.12	Application of mechanical strain to microwires. The left probe is held in a fixed position and the right probe is moved incrementally towards it using the x-direction control dial on the probe manipulator. The silicon wire experiences strain and this induces a bend deformation in the wire. . . .	53
4.1	Under no applied strain.	56
4.2	Under an applied bending strain of 2.9%.	56
4.3	The current response of Sample 2 of the Set A concentration microwires, for both unstrained and strained (1.7%) trials at a set bias of 0.2 V. . . .	57
4.4	Sample 1 under no applied strain.	58
4.5	Under an applied bending strain of 2.4%.	58
4.6	The fractional change in resistivity plotted as a function of strain for four individual wires in Set B, showing consistent trends with an average slope of -14 ± 3 , which corresponds to the gauge factor for this set.	59
4.7	The electrical response of a degenerately doped microwire in response to strain. The arrow indicates the direction of increasing applied strain, from 0% to 2.2%.	61
4.8	A direct comparison between the three sets of doped n-type microwires shows an appreciably stronger response for the more highly doped wires (Set C) than for either set of wires with doping concentration on the order of 10^{17} cm^{-3} (Sets A and B).	63
4.9	Schematic showing the series resistance components of the overall microwire/polymer system. A reduction in any of the five resistive components will result in a reduction in overall resistance.	65

List of Copyright Material for which Permission was Obtained

Figure 3.1 Copyright AIP Publishing LLC 2007 10.1063/1.3178556

Figure 2.9 Copyright Cambridge University Press 2014 10.1557/jmr.2014.52

Abbreviations

Ag	Silver
CCI	Center for Chemical Innovation
CVD	Chemical Vapour Deposition
DI	Deionized
FTO	Fluorine-doped Tin Oxide
HER	Hydrogen Evolution Reaction
HPLC	High Performance Liquid Chromatography
ITO	Indium Tin Oxide
KOH	Potassium hydroxide
LCOE	Levelized Cost of Energy
OER	Oxygen Evolution Reaction
PR	Piezoresistive
PVD	Physical Vapour Deposition
RTA	Rapid Thermal Anneal
SEM	Scanning Electron Microscopy
W	Tungsten

Physical Constants

Boltzmann's Constant	k	$=$	$1.380\,064\,88 \times 10^{-23} \text{ m}^2 \text{ kg s}^{-2} \text{ K}^{-1}$
Electron Mass	m_e	$=$	$9.109\,382\,15 \times 10^{-31} \text{ kg}$
Faraday's Constant	F	$=$	96485 C mol^{-1}
Elementary Charge	e	$=$	$1.602\,176\,565 \times 10^{-19} \text{ C}$
Speed of Light	c	$=$	$2.997\,924\,58 \times 10^8 \text{ ms}^{-1}$

Chapter 1

Introduction

1.1 Motivation

1.1.1 Solar Energy

The world's population is growing steadily. By 2050, it is projected to surpass 8 billion [1]. As more and more people fill the planet, energy demands grow too; and the correlation is not necessarily linear. In fact, worldwide energy use per capita has been increasing significantly over the past decade, growing from 1752 kg of oil equivalent (kgoe) in 2004 to 1890 kgoe in 2011 [2]. Not only are there more people on Earth than ever before, but individual people are demanding more energy every year. This is due in part to the consistent increase in standard of living within rapidly developing nations such as China and India, where growing populations combine with increased per capita energy demand.

Currently, over 80% of worldwide energy consumption is satisfied using non-renewable fossil fuels like coal and petroleum. This puts huge strain and demand on quickly-depleting resources [2]. Excessive use of fossil fuels also increases the amount of CO₂ in the atmosphere, a main contributor to global climate change [3]. Global carbon dioxide emissions have increased significantly since the mid-1950s, and continue to rise [4]. It is clear that a reduction in dependence on fossil fuels is a critical area of modern research. In order to maintain the quality of life and level of energy consumption that people have come to expect, there needs to be a significant shift away from non-renewable processes towards a reliable, renewable solution. And this change needs to be implemented soon.

The solar flux that hits the Earth's surface equates to 1367 W per m² [5, 6]. This amount of power could be harvested to provide the planet with a sustainable energy source that will last indefinitely. Photovoltaics is a branch of energy science that looks at the direct conversion of sunlight into a usable source of electrical energy. It is based around the physical phenomenon of the photovoltaic effect, wherein a photon incident on a material frees bound electrons, allowing for electric current through the material. Photovoltaic cells have been around for a long time, with the first silicon solar cell reported in 1941 [7]; but they have traditionally had poor conversion efficiency, with even very recent modules exhibiting only 25% efficiency under one-sun conditions [8]. Solar cells are therefore currently less economically viable than other methods of electricity production, with an estimated levelized cost of energy (LCOE) of \$297 (USD) per MWh, as compared to coal at \$49 per MWh and nuclear power at \$64 per MWh [9]. This, combined with energy

storage problems, have set solar cells' stock back as a viable candidate for large-scale replacement of fossil-fuel dependent energy production.

Despite these concerns, interest in photovoltaics has experienced a resurgence in recent years, as public awareness of the necessity of renewable energies has grown. More research efforts have been focused on improving device efficiency and economic feasibility. Some forecasts predict that under a positive-policy model, the market for utility-scale photovoltaic systems could quadruple from 2012 - 2017 [10]. However, large scale adoption of solar energy will require addressing two main issues: photovoltaic efficiencies and energy storage. The harvesting of solar energy by photovoltaics fluctuates with seasonal as well as daily changes in sunlight levels, and energy harvested in ideal conditions cannot as of yet be efficiently stored for later use. A potential solution to this constancy problem lies in the storage of energy in the form of chemical fuels, such as hydrogen. If the solar energy reaching the earth's surface could be harnessed and used to produce chemical fuels, then these fuels could then be stored and transported for use as secondary energy sources [6].

1.1.2 Hydrogen Fuel

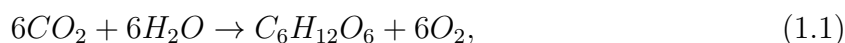
Hydrogen fuel is extremely promising as a chemical fuel. It is cleanly consumed in combustion engines and fuel cells, producing no carbon emissions and no byproducts except for pure water. In 2011, \$38 million was spent on hydrogen and fuel cell energy research in Canada [11], highlighting the growing interest in hydrogen as a chemical fuel. But unlike oil, coal and other currently used fossil fuels, hydrogen does not naturally exist

in H₂ form on the Earth's surface. In order to capitalize on hydrogen's potential as a chemical fuel, a cost-effective method of producing hydrogen must be developed.

Currently, the main impediment to the production of pure hydrogen is economic. Using proven methods of hydrogen production such as coal gasification and nuclear thermal splitting, the cost of production, in currency as well as energy input, is non-competitive when compared with equivalent outputs of gasoline. The overall cost in 2006 dollars, including production, transportation and dispensing, for coal-gasification produced hydrogen was estimated to be approximately \$1.91 per gallon of gasoline equivalent (gge); for nuclear thermal splitting, it was estimated at \$2.22/gge. In comparison, the production, transport and dispensing of a gallon of gasoline was approximately \$1.12 [6]. Solar power has the potential to provide a near-limitless and sustainable source of energy for production of hydrogen, if it can be economically and efficiently harnessed.

1.1.3 Artificial Photosynthesis

In recent years, artificial photosynthesis has drawn significant interest in the pursuit of an efficient and economical method of producing hydrogen fuel [12, 13]. The term refers to the process performed by plants as they chemically convert carbon dioxide and water into the carbohydrate sugars needed to drive their growth and function (Figure 1.1). The chemical process requires sunlight as an energy source to perform the reaction



where oxygen is a waste product of the process. Artificial photosynthesis mimics this process using semiconductor materials to facilitate the absorption of light (Figure 1.2). Instead of creating sugar from carbon dioxide and oxygen inputs, artificial photosynthesis evolves pure hydrogen through electrolysis of the water molecule H_2O .

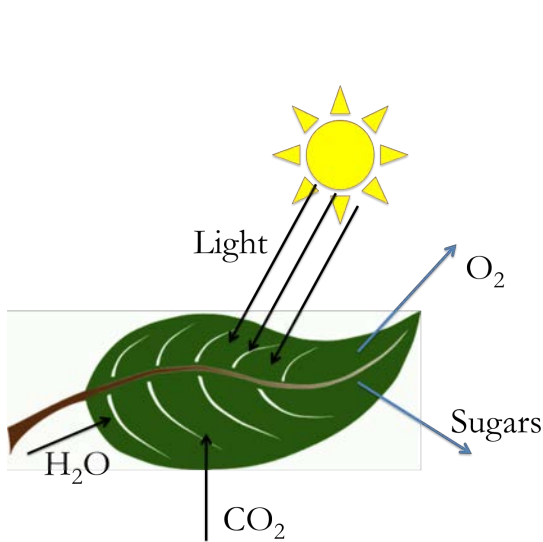


FIGURE 1.1: Photosynthesis is the natural process by which plants convert light energy, water, and carbon dioxide into the carbohydrate sugars required to drive their growth and function. Oxygen is a waste product of this process. The proposed device aims to mimic this process.

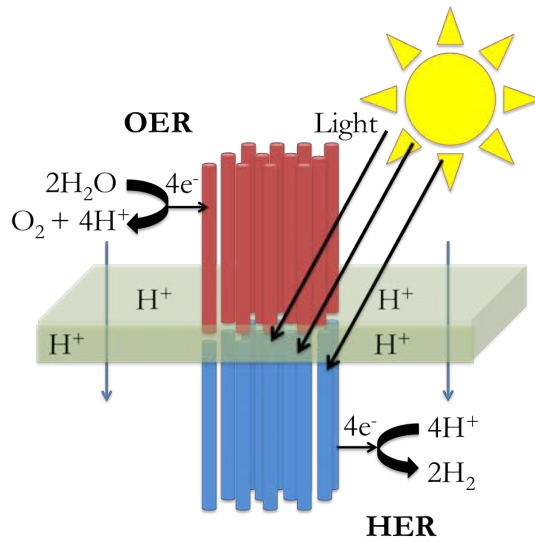
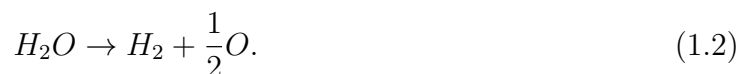


FIGURE 1.2: The proposed artificial photosynthesis device will be comprised of two arrays of silicon microwires embedded in a proton-permeable membrane. On the anode side (n-type), O_2 will be evolved; on the cathode side (p-type), H_2 will be evolved and captured.

Electrolysis of water is the electrochemically-driven splitting of water into its components, hydrogen and oxygen. This process can successfully produce molecules of H_2 , following the reaction



The energy required to perform this conversion, per molecule of water split, is 1.23 eV. In artificial photosynthesis, this energy is provided by incident sunlight, and the collection of the required energy and production of hydrogen occur within the same integrated device, reducing transport cost and energy transfer losses. In order for the sunlight absorbed by a semiconductor to successfully drive this reaction, the semiconductor must be capable of absorbing light with energies in excess of 1.23 eV (wavelengths $\leq 1000\text{nm}$), since some energy is unavoidably lost to carrier recombination and kinetic overpotential (internal losses occurring when driving the hydrogen and oxygen evolution reactions). In order to mitigate the effect of these losses, it is reported that supplying energy between 1.6 - 2.4 eV is enough to successfully drive the reaction while accounting for energy lost to external effects [13].

The artificial photosynthesis device design proposed by Lewis et al [13] incorporates two arrays of semiconductor microwires that are capable of absorbing sunlight and facilitating the water-splitting reaction. On the anode side, n-type material absorbs incident light to produce a photocurrent which drives an oxygen evolving reaction (OER). High-aspect ratio structures like microwires increase light absorption and reduce potential for carrier recombination in the material bulk. An array of these wires will be embedded in a transparent, proton-permeable membrane which allows transport of cations to the cathode side. The photocathode will be made up of p-type microwires, and through light absorption, provide the cathode current necessary to drive the hydrogen evolution reaction (HER). Both microwire arrays will be coated with metallic catalysts which aid in charge transport

across the semiconductor-liquid junction by lowering the required overpotential, improving kinetics and efficiency of the chemical reaction. In keeping with the large-scale vision of an affordable project, the catalysts will be selected in order to optimize performance while minimizing cost, and must therefore be comprised of earth-abundant materials. The catalyst coating on the microwire surface must be thin or discrete enough to allow transparency so that effective light absorption can still take place. This is achieved by using nanoparticulate globules of catalyst deposited on the surface of the microwire. For research purposes, n-type and p-type silicon can facilitate a model of the dual bandgap p-n system, providing a proof-of-concept means of investigating the mechanism of solar-driven electrolysis.

The n-type wires that make up the photoanode must be both efficient in photon conversion to charge carriers, and stable in the aqueous environment comprising the artificial photosynthesis cell. The potential for energy losses through the course of the conversion is very high, and therefore known solar-to-chemical fuel efficiencies in this artificial photosynthesis cell design are currently low. It is estimated that a dual-bandgap model comprising n-type and p-type semiconductors will exhibit 15% solar-to-hydrogen efficiency when accounting for parasitic losses [13]. Due to these efficiency issues, the widespread adoption of a device of this kind is still far from realization. Selection of materials and reduction of integral energy losses are key areas of research that seek to improve device efficiency and economic viability. To illustrate, the amount of surface area required to run one average household using integrated artificial photosynthesis devices can be roughly estimated.

The average Canadian household consumes approximately 33 kWh of energy per day [14]. The energy density of hydrogen is around 33.3 kWh/kg. So, a household running solely on hydrogen fuel cells would require about 1 kg of hydrogen gas per day. However, fuel cells are not 100% efficient in their conversion of hydrogen to power; most commercial fuel cells operate at about 65% efficiency [15], increasing the amount of hydrogen required to 1.52 kg. It is possible to roughly determine the amount of surface area covered by the integrated solar device that would be necessary to power an isolated household with this model. The current model as envisioned by [12, 13] can pass a current density of 20 mA/cm² based on average solar intensity. Assuming 100% conversion efficiency, and employing Faraday's laws of electrolysis,

$$m = \frac{ItM}{Fz}, \quad (1.3)$$

where m is the mass produced, I is the constant current passed for time t , F is Faraday's constant, defined as 96485 C mol⁻¹, M is the molar mass of hydrogen and z is the number of electrons transferred per mole [16], the output of H₂ gas per m² produced will be 360 g per day. In order to produce the required 1.52 kg of hydrogen necessary to run their home, the average Canadian homeowner would need to have room for 4.2 m² of panels of this device. These panels would need to be situated in areas of maximum sunlight (for a Canadian household, this would likely mean on a south-facing rooftop) and with close access to pressurized receptacles to store the produced hydrogen gas. This is an attractive prospect when considering it in conjunction with other methods of energy production,

or for buildings in remote locations that are necessarily off-grid. It offers a solution to the problem of how to store excess energy during periods of intense sunlight so that that energy can be used when it is needed. However, in terms of current efficiencies it is also a gross exaggeration. Incorporating the model solar-to-hydrogen efficiency predicted by [13] would reduce the amount of H_2 produced per m^2 per day to only 54 g – which would cause the homeowner to require 28.4 m^2 of panels to power their house. This makes abundantly clear the importance of improving device efficiency.

In this study there is a focus on efficiency improvement achieved through reducing voltage drop in the microwire-polymer system. Figure 1.3 shows a unit cell of the discussed artificial photosynthesis device, with an n-type wire to represent the photoanode, embedded in a polymer membrane in series with a p-type wire to represent the photocathode. The IR drop across this system is a significant source of voltage drop in the scope of the device. Any reduction in the resistivity of the microwires or polymer, or in the resistance of the

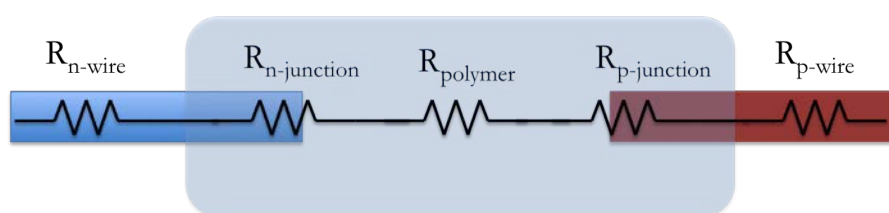


FIGURE 1.3: Overall system resistance of a unit cell of the microwire/polymer/microwire system. Reducing the resistance of any of the components will help to reduce voltage drop across the system and increase efficiency.

junction between the wires and the polymer, will be beneficial in reducing the voltage drop across this system [17]. This work focuses on the potential of reducing the resistivity of the n-type microwires specifically (the photoanode component of the system). Silicon

has been selected as a material for prototypical study of the artificial photosynthesis device due to its abundance and because it is well understood.

Studies have shown that doped silicon structures exhibit a piezoresistive response to increasing strain [18–20]. This indicates that it may be possible to reduce the electrical resistance of silicon microwires by applying continuous physical strain to their crystalline structure. Applied strain may also have an effect on the optoelectronic properties of the microwires, which, while not a focus of this thesis, is an interesting avenue for future study on this system [21, 22]. The feasibility of applying piezoresistance as a potential means of increasing the electrical performance of the silicon microwires grown and designed for inclusion in the artificial photosynthesis project is herein investigated.

1.2 Thesis Outline

In the body of this thesis, the theoretical background that underpins this study will be outlined, specifically regarding silicon and its unique piezoresistive properties, as well as the specific electrical behaviour of n-type doped silicon under strain. This section will also investigate the body of literature that exists which have reported on studies of the differing piezoresistive responses exhibited by different doping concentrations, length scales, and surface functionalizations for silicon microwires. The difference between the response of bulk silicon and silicon structures on the micro-scale is also investigated. A model is developed for the application of strain to the microwires and its comparison

to the fractional change in resistivity using the gauge factor. The experimental design is then detailed, involving the selection of specific n-type microwires for analysis, the preparation of samples for analysis, and the developed methods of electrically testing the individual microwires to determine their resistance under stress. In the results and discussion section, results for three sets of differently-doped, n-type silicon microwires are presented and the physical causes of these results are discussed. The potential impact of improving the microwires' electrical resistance on the overall design for the artificial photosynthesis device is also outlined. In the final chapter of this work, a conclusion is drawn summarizing the response of n-type crystalline silicon microwires with differing doping levels under applied strain, and the feasibility of harnessing this effect to aid in efficiency improvement within the integrated artificial photosynthesis device.

Chapter 2

Background Theory

2.1 Piezoresistivity of Silicon

Silicon has been shown to be a piezoresistive material [18]. This means that the application of mechanical stress to silicon will have an effect on its conductivity. The “gauge factor” quantifies the sensitivity of a particular material’s resistance to an applied strain. The gauge factor is comprised of two terms, one a geometrical contribution, and one a measure of the sensitivity of resistivity to strain, as given by

$$GF = (1 + 2\nu) + \frac{(\delta\rho/\rho)}{\epsilon_a}, \quad (2.1)$$

where ν is Poisson’s ratio (the negative ratio of transverse to axial strain), ρ is the resistivity of the material, and ϵ_a is the applied axial strain. The overall change in

resistance can be derived from the definition of resistance, given by

$$R = \frac{\rho L}{A}, \quad (2.2)$$

where R is the resistance, ρ the resistivity, L the length of the wire, and A the cross-sectional area of the wire. A change ΔR in the resistance can result from a change in a) the resistivity of the material; b) the length of the wire; and/or c) the cross-sectional area of the wire [23]. Differentiating gives

$$\frac{dR}{R} = \frac{d\rho}{\rho} + \frac{dL}{L} - \frac{dA}{A}. \quad (2.3)$$

The ratio of the change in length L and the original length is the axial strain, ϵ_a , referring to an applied force in the axial plane which causes a geometrical change, as shown in Figure 2.1. The fractional change in the cross-sectional area, A , can be further reduced

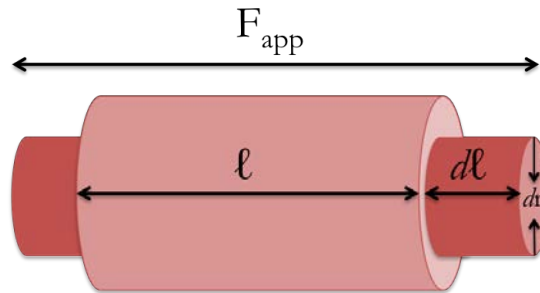


FIGURE 2.1: Geometric deformation of a cylinder under an applied force.

to

$$\frac{dA}{A} = \frac{d(\pi(D/2)^2)}{A} = \frac{2dD}{D} \quad (2.4)$$

where D is the cross-sectional diameter. The change in diameter over original diameter is known as the traverse strain, ϵ_t . Incorporating the definitions of traverse and axial strain into equation 2.3 gives

$$\begin{aligned}\frac{dR}{R} &= \frac{d\rho}{\rho} + \epsilon_a - 2\epsilon_t \\ \frac{dR/R}{\epsilon_a} &= \frac{(\delta\rho/\rho)}{\epsilon_a} + \left(1 - \frac{2\epsilon_t}{\epsilon_a}\right).\end{aligned}\tag{2.5}$$

The negative ratio of traverse to axial strain is known as Poisson's Ratio, ν . This can be substituted into 2.5 to produce

$$\frac{dR/R}{\epsilon_a} = \frac{(\delta\rho/\rho)}{\epsilon_a} + (1 + 2\nu),\tag{2.6}$$

which gives the definition of the gauge factor as

$$GF = \frac{dR/R}{\epsilon_a}.\tag{2.7}$$

In a conductor such as a metal, the dominant contribution to the gauge factor is the macroscopic change in geometry caused by applying tensile or compressive stresses (the first term in equation 2.1), as illustrated in Figure 2.1. The strain sensitivity term is typically vanishingly small. However, in a semiconductor such as silicon, this strain sensitivity factor has a much greater effect on the overall gauge factor than the geometrical contribution, and so the geometrical term can usually be neglected [24], giving

$$GF = \frac{(\delta\rho/\rho)}{\epsilon_a}\tag{2.8}$$

as the gauge factor for a semiconductor such as silicon. This term can be extended to define the piezoresistive coefficient, Π , of the material. The piezoresistive coefficient is the relative change in resistivity over the applied stress,

$$\Pi = \frac{(\Delta\rho/\rho)}{X}, \quad (2.9)$$

and has units of Pa^{-1} . Here X is defined as the applied stress, $X = Y\epsilon_a$, where Y is Young's modulus for the material in question.

2.1.1 Young's Modulus

Young's modulus is a measure of a material's elastic stiffness, and characterizes how a material will deform under an applied strain. Equation 2.9 illustrates that the gauge factor and piezoresistive coefficient are related by a factor of the Young's modulus. For the single-crystal silicon that is the focus of this thesis, Young's modulus depends strongly on the sample's crystalline orientation. Recent reports state that for (111) oriented single-crystal silicon, the Young's modulus is transversely isotropic and approximately 188 GPa [25].

A variation in Young's modulus with doping concentration of silicon has been reported [26]. This report was focused on p-type silicon and proposed a 20 - 30% increase in the Young's modulus between undoped (intrinsic) and highly doped ($\sim 10^{19} \text{ cm}^{-3}$) silicon,

with a reported accuracy within 15 - 20%. More recent studies have found that the variation in Young's modulus between lower-doped silicon ($\sim 10^{15} \text{ cm}^{-3}$) and degenerately doped silicon ($\sim 10^{20} \text{ cm}^{-3}$) is only on the order of 1 - 2% and is therefore negligible for most calculations [25, 27].

2.1.2 Strain in a Crystalline Lattice

In a normal environment and under no applied stress, isotropic materials will exhibit a consistent resistivity when exposed to an electric field in any direction along their axes [28]. A change in resistivity in a certain direction can be achieved by applying a stress to the isotropic lattice, deforming its structure. The nature of this deformation depends on the plane of the stress' application and its action (tensile or compressive). Single-crystalline silicon is an anisotropic structure (see Figure 2.2); therefore, its resistivity for a given applied field will depend on the direction of current flow with respect to its crystalline orientation. By extension, a change in resistivity can occur when the single-

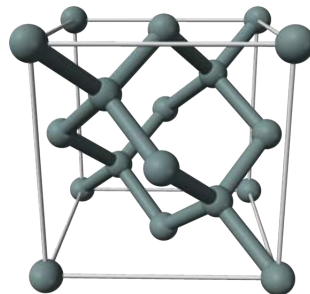


FIGURE 2.2: The diamond cubic lattice form of single-crystalline silicon.

crystalline silicon is subjected to mechanical stress on its lattice. However, the specificity of this change will depend on the direction of application of the strain with respect to

silicon's lattice structure. Solid state theory predicts how the transport of charge carriers (electrons and holes) will be affected by the change in lattice structure induced by the applied stress.

In order to understand how deformation of the lattice structure affects the transport of charge carriers in a semiconductor, it is necessary to take a quantum mechanical approach. A basic representation of a one-dimensional crystalline lattice is provided by the Kronig-Penney model [29]. This model describes an infinite, one-dimensional crystal lattice as a series of square potential barriers of width b , separated by the lattice parameter a . It is illustrated in Figure 2.3.

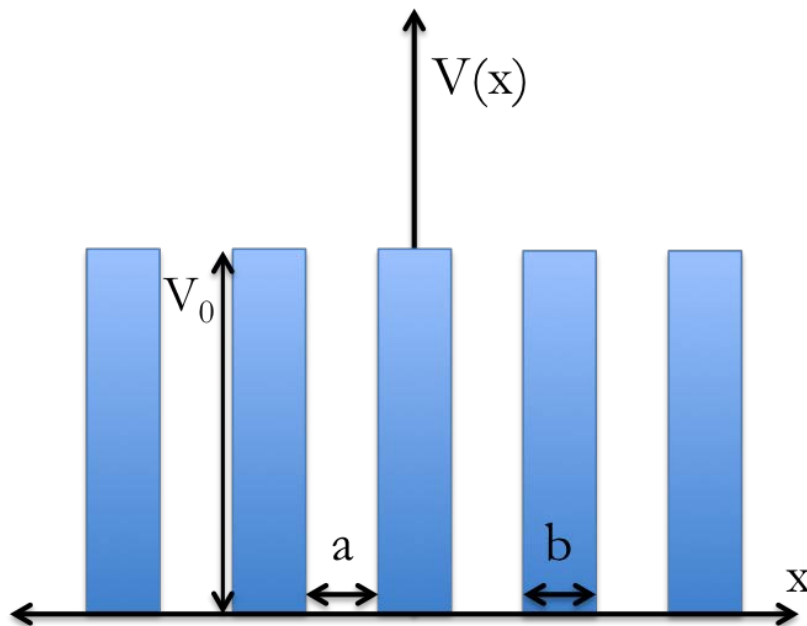


FIGURE 2.3: The Kronig-Penney model represents a one-dimensional crystal lattice as a periodic array of potential wells, where a is the interatomic spacing and b the barrier width.

A free electron incident on the lattice will occupy the energy states allowed by the solution of the time-independent, one-dimensional Schrödinger equation

$$E\Psi = \hat{H}\Psi, \quad (2.10)$$

where the Hamiltonian \hat{H} in this case is defined as

$$\hat{H} = \frac{-\hbar^2}{2m} \frac{d^2}{dx^2} + V(x) \quad (2.11)$$

and $V(x)$ is defined as the periodic potential

$$V(x) = A \sum_{n=-\infty}^{\infty} \delta(x - na), \quad (2.12)$$

where A is the area of the potential barrier of width b and a is the interatomic spacing.

The analytical solution for this case is given by

$$\cos(ka) = \cos(\alpha a) + \frac{P}{\alpha a} \sin(\alpha a), \quad (2.13)$$

where k is the wavevector, P is equal to $\frac{mAa}{\hbar^2}$ and α is defined as $\frac{\sqrt{2mE}}{\hbar}$ [29, 30]. The relationship between wavevector k , which describes the wave, and energy E of the carrier is called the dispersion relationship, and its dependency on a is illustrated in Figure 2.4, for a case where the original, unstrained lattice parameter a is 5\AA and the area of the barriers is 3.1 eV [29, 31]. The dispersion relationship illustrates the dependency of a crystalline material's energy bandgap structure on strain. When mechanical strain is applied, the

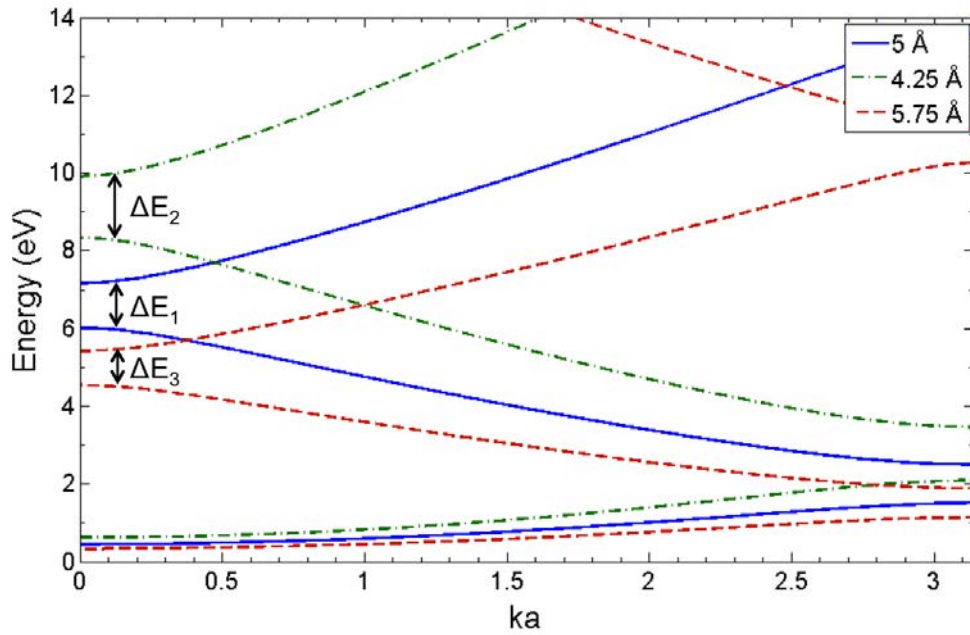


FIGURE 2.4: An example dispersion relation for the Kronig-Penny model in a silicon lattice with original, undeformed interatomic spacing 5\AA , continuous across allowed and forbidden energies. Shortening the interatomic spacing a will increase the bandgap; lengthening it will decrease the bandgap. This is illustrated here as $\Delta E_3 < \Delta E_1 < \Delta E_2$, where ΔE_3 corresponds to 15% increase in a and ΔE_2 to a 15% decrease. These strain values are extreme and are used for the purpose of illustration only. Figure plotted in MATLAB.

lattice parameter a changes. The direction of this change will depend on the mechanism of applied strain, with a compressive strain resulting in a smaller interatomic spacing and a tensile strain resulting in a larger interatomic spacing. This, of course, will change the overall periodicity of the crystal, resulting in a change in carrier mobility through the lattice. The carrier mobility will affect the resistivity of the material, as defined by

$$\rho = \frac{1}{n\mu q}, \quad (2.14)$$

where μ is the carrier mobility, q is the absolute value of the electronic charge, and n is the number of charge carriers. If the mobility of carriers is changed following a change

in interatomic spacing, the resistivity ρ will correspondingly change following the inverse relationship. An application of tensile strain will increase interatomic spacing, increasing mobility and decreasing resistivity; an application of compressive strain will decrease the interatomic spacing, decreasing mobility and increasing resistivity, for those cases in which the majority charge carriers are electrons. Physically, this can be explained by overlap between interacting orbitals in the lattice; as interatomic spacing is decreased, orbitals of atoms in the lattice interact more, reducing mobility of electrons in those regions. The opposite occurs for increased lattice spacing [32, 33].

2.1.3 Doped Silicon

The specific mechanism of silicon's electrical strain sensitivity will depend not only on its crystalline orientation with respect to the applied field, but also on its dopant type. In order to artificially increase the conductivity of the material, silicon can be doped with impurities that change the ratio of electrons to holes according to the desired response to an applied field. The addition of a dopant impurity will increase the conductivity of silicon; however, the mechanism is different based on whether the added impurity is an electron donor or an electron acceptor. To understand the effect of adding dopant impurities to a semiconductor, a brief discussion of the Fermi level is warranted. The number of occupied electron states in a material is dominated by the Pauli exclusion principle, which states that no energy state can be occupied by two identical electrons. If two electrons occupy the same energy state, they must necessarily have opposite spins.

This principle underpins the Fermi-Dirac distribution,

$$F(E) = (1 + \frac{e^{E-E_F}}{kT})^{-1}, \quad (2.15)$$

which defines the number of states that contain electrons for a given energy E at a given temperature T , where k is defined as Boltzmann's constant, $1.38 \times 10^{-23} \text{ m}^2 \text{ kg s}^{-2} \text{ K}^{-1}$. The parameter E_F is the Fermi level [34]. The Fermi level is defined to be the point at which the probability of an electron occupying a given state is $1/2$, or

$$F(E)_{E=E_F} = \frac{1}{2}. \quad (2.16)$$

As the temperature is incrementally increased, the energy of the material's carriers will be increased by a factor kT . An increase in temperature excites the electrons, and as the temperature is continually increased, the proportion of excited electrons grows correspondingly [34, 35].

The Fermi level in a metal at absolute zero is illustrated in Figure 2.5. In a semiconductor, the Fermi level exists in the forbidden gap between the valence and conduction bands (Figure 2.6). A valence-band electron must be able to gain enough energy to overcome the bandgap in order to be excited into the conduction band. This characteristic is what distinguishes a highly conductive metal from a semiconductor. Insulators have bandgaps even larger than those of semiconductors, reducing the possibility of feasibly exciting an electron to the conduction band, and so reducing the material conductivity.

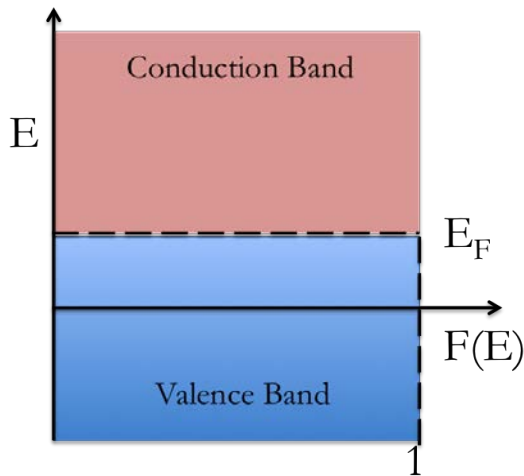


FIGURE 2.5: The Fermi level at absolute zero in a metal. All occupied states exist below the Fermi level at this temperature.

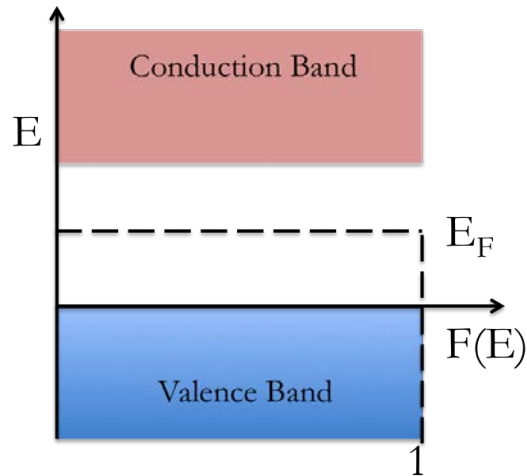


FIGURE 2.6: The Fermi level at 0K in a semiconductor, located in the forbidden region between valence and conduction bands.

Doped silicon exhibits higher conductivity than intrinsic silicon. There are two types of doped silicon: n-type, in which an impurity is added to increase the proportion of electrons in the material (a “donor” impurity); and p-type, in which an added impurity increases the proportion of electron-holes in the material (an “acceptor” impurity). These distinct dopant types will have very different effects on the proportion of minority and majority charge carriers within the silicon, which will change the conductivity of silicon and correspondingly its piezoresistive response. The Fermi level diagram of n-type doped silicon is shown in Figure 2.7 [36]. The increase in electrons in the conduction band shifts the Fermi level closer to the conduction band and conductivity is increased.

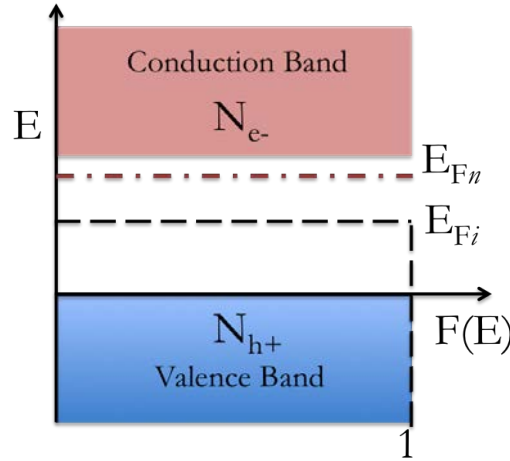


FIGURE 2.7: Band diagram for n-type doped silicon showing the Fermi level of intrinsic silicon (E_{Fi}) and the shift in the Fermi level (to E_{Fn}) resulting from the addition of dopant impurities to the intrinsic silicon. This causes a surplus of electrons in the conduction band in comparison to holes in the valence band ($N_{e-} > N_{h+}$), which shifts the Fermi level of the material.

2.1.4 Strained n-Si

The microstructures investigated in this study are composed of n-type silicon, that is, silicon doped with a donor impurity such as phosphorus. The behaviour of n-Si under strain is a complicated process involving a change in the effective mass of the electrons. In order to understand the mechanism of this change, a more fully developed model for n-Si's bandgaps need to be employed. The commonly-used band gap model for a semiconductor such as silicon is a many-valley model, referring to the number of band-edge points predicted by the model. It posits that silicon's band structure is more complicated than the simple form consisting of a band-edge with a constant spherical surface energy [23, 30, 37]. The behaviour of silicon's band gaps under strain is called the charge transfer model [37], and it is the basis of piezoresistive behaviour in n-type silicon.

Six ellipsoidal “valleys” make up the band structure of single-crystalline silicon, and these valleys are so-called due to the existence of electrons of two effective masses; one of these effective masses corresponds to the major axis of the ellipsoidal band (m_{\parallel}), and the other to the minor axis (m_{\perp}) [23]. The mobility of carriers are dependent on their effective mass. Carrier mobility is defined by

$$\mu = \frac{v_d}{E}, \quad (2.17)$$

where v_d is the carrier drift velocity and E is the electric field experienced by the carrier. Carriers with a lower mobility are so described because the transport of these carriers through a given electric field is lower than for those carriers with higher mobility. Thus, carriers with a lower mobility appear to have a higher effective mass than carriers with higher mobility. Mobility is related to the effective mass by

$$\mu = \frac{q}{m^*} \tau, \quad (2.18)$$

where q is the absolute value of the electronic charge, m^* is the effective mass of the electron, and τ is the average time between collisions of carriers with other carriers and with the lattice [34]. The effective mass, in this case, is not necessarily the constant mass of a free electron, given by 9.11×10^{-31} kg. The effective mass depends on the electron’s interaction with atoms in the crystalline lattice, and is defined to be

$$m^* = \hbar^2 \left(\frac{\delta^2 E}{\delta k^2} \right)^{-1}, \quad (2.19)$$

where k is the wavevector and E the energy. In a one-dimensional lattice model such as the Kronig-Penny model described in Section 2.1.2, the effective mass can be defined as

$$m^* = \frac{\hbar^2}{2Aa^2} \text{sec}(ka), \quad (2.20)$$

where a is the interatomic spacing, A the area of the potential barriers, and k the wavevector [34]. So the effective mass of a carrier is dependent on the interatomic spacing in a uniform lattice, and on its position in reciprocal space; and the mobility of a carrier is dependent on its effective mass; and, referring back to Equation 2.14, the resistivity of a material is dependent on the mobility of its carriers. From this theory the model of n-silicon under strain can be developed.

Note that in the many-valley model, $m_{\parallel} > m_{\perp}$; so the electrons corresponding to the major axis are known as heavy carriers (low mobility), while the electrons corresponding to the minor axis are known as light carriers (higher mobility). Under zero applied strain, the major and minor axes are equally populated, and the proportion of heavy and light electrons is equivalent. However, when compressive strain is applied in a given direction, an energy shift occurs, facilitated by the change in lattice structure described previously. Due to a decrease in the carrier mobility caused by a decrease in interatomic spacing a , the valleys with major axes aligned parallel to the strain application are reduced in energy. This incites a transfer of electrons into these valleys from the valleys with major axes perpendicular to the applied strain, causing an imbalance in effective mass. There is now an excess of “heavy” electrons oriented longitudinally with respect to the applied

strain (see Figure 2.8).

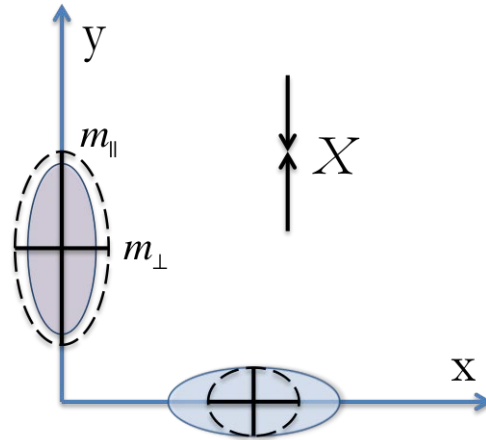


FIGURE 2.8: A shift in the ratio of heavy to light carriers occurs when the lattice undergoes compressive strain. Compressive strain along the y axis induces a transfer of electrons from the transverse valleys to the longitudinal valleys, increasing the proportion of heavy carriers in the y -direction and therefore reducing mobility and conductivity. The solid ellipses indicate the original form of the valleys; the dashed ellipses, the valleys under strain X .

This excess of heavy electrons increases the resistance to current in that direction, so the application of compressive strain will cause an increase in resistance (and, correspondingly, a decrease in conductance) along the axis of propagation of the applied strain in n -type silicon [37]. The transfer of electrons will occur until the population of electrons in the transverse states has been exhausted; at this point, the change in resistance along the longitudinal direction is saturated and no additional effect will result from increasing the strain further, as shown in Figure 2.9 from [30].

The opposite occurs for tensile strain; the longitudinally-oriented valleys are shifted up

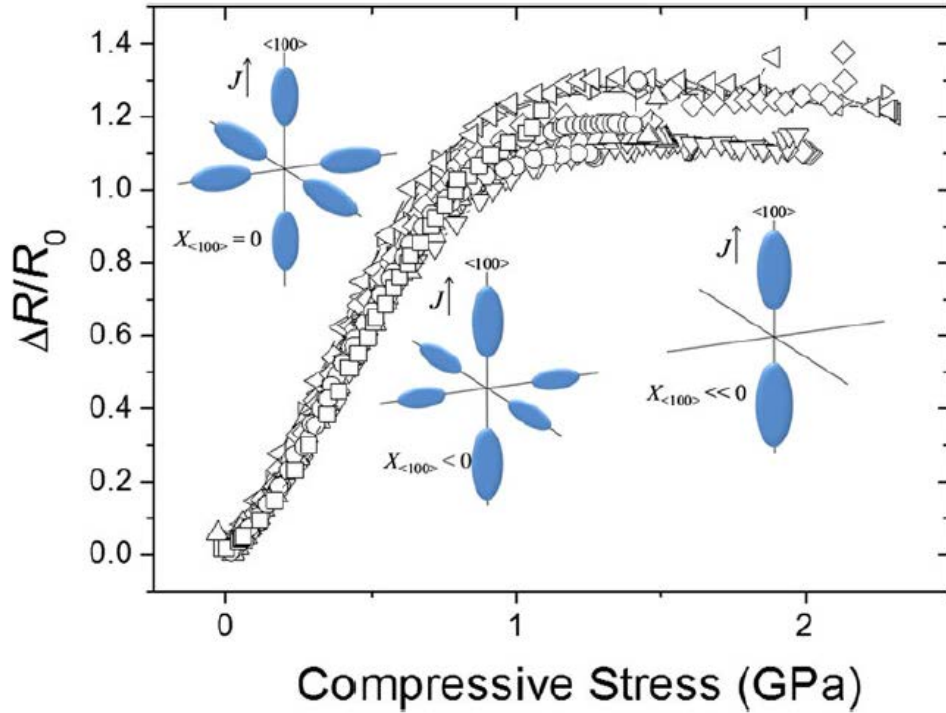


FIGURE 2.9: The effect of increasing compressive strain on the valley structure of silicon. When no strain ($X = 0$) is applied, the proportion of heavy and light carriers is equivalent. As compressive strain is increased ($X < 0$), a charge transfer increases the proportion of heavy carriers oriented longitudinally with respect to the strain. This increases resistance until the point of saturation ($X \ll 0$). Copyright 2014 by the Cambridge University Press. Used with permission.

in energy due to a shortened band gap, promoting a transfer of electrons out of the longitudinal valleys into the transverse valleys, which causes a higher proportion of light carriers in the longitudinal direction. This decreases longitudinal resistance and increases conductance.

2.2 Direct Ohmic Contact to Silicon

The studied microwires have a diameter of about $1.5 \mu\text{m}$, which makes it very difficult to form ohmic contact to the wires using the traditionally accepted methods within an electrical probing station. Typical methods of forming electrical contact involve the deposition of a metal directly to the silicon surface via sputtering or thermal evaporation. As the wires are so small, the process used for metal contact deposition would likely be electron beam PVD (physical vapour deposition), which requires high vacuum and greatly increases the complexity of electrically testing a single wire. As such, in this study a more direct method of forming ohmic contact was used. It has been noted that the application of specific, local mechanical pressure will induce a phase transition in crystalline silicon [38, 39].

When local pressure of approximately 11 GPa is applied to crystalline silicon, the silicon directly underneath the pressure undergoes a phase transition to form Si-II, which is a metallic phase of silicon that is unstable at standard temperature and pressure. As long as local pressure is consistently applied, the crystalline silicon will remain in this metallic phase, creating a viable ohmic contact in this region. As soon as the pressure is relaxed, the silicon reverts to its semiconducting Si-I phase. This characteristic was exploited in order to make direct, repeatable and non-destructive ohmic contact to the silicon microwires using tungsten probes. A second phase change from Si-II to Si-V has been shown to occur between 16 and 18 GPa [39, 40]. However, this amount of pressure

was not shown to be achievable using a single probe (see Section 3.2.1).

2.3 Mechanical Strain Model

A silicon microwire undergoing deformation can be modeled as a beam of circular cross-section undergoing pure bending. From [41], the radius of curvature r_c can be defined, which describes the degree of bend of a wire. An object experiencing tensile or compressive

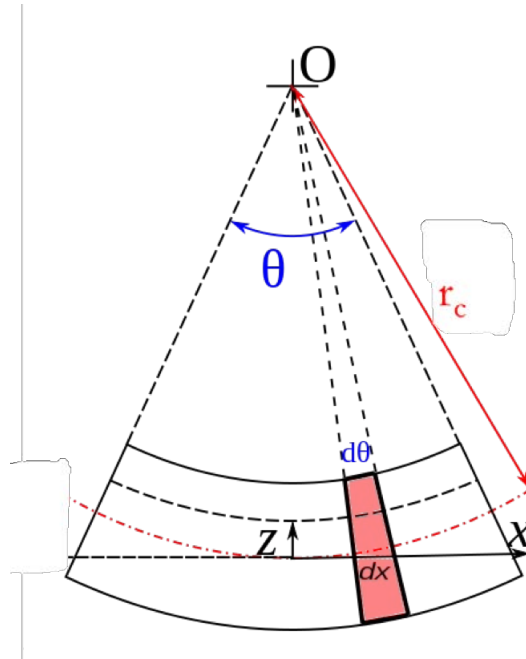


FIGURE 2.10: Geometric illustration of element of bent wire, where r_c is the radius of curvature, θ the angle, and z the distance between the neutral axis and the point of measurement.

force is said to be undergoing strain, which is defined as the change in the length of the object (in the plane of the applied force) over the original length, or

$$\epsilon = \frac{\Delta L}{L}. \quad (2.21)$$

When a beam is purely or uniformly bent, one side is compressed while the other is extended; essentially, the beam's physical length is shortened on one side and lengthened on the other. There exists a neutral axis in which the beam's length remains the same as that of the original, undeformed beam. When calculating the change in length, we define z to be the distance between the neutral axis and the point of measurement (see Figure 2.10). For a beam of uniform circular cross section, the neutral axis can be found to propagate along the central axis of the cross-section [41]. The length of the neutral axis (in other words, the original, undeformed length of the wire) can be defined as

$$L_o = r_c \theta, \quad (2.22)$$

where r_c is the radius of curvature of the wire segment and θ is the central angle. The length after deformation, then, is defined as

$$L = (r_c - z)\theta, \quad (2.23)$$

where, again, z is the distance from the neutral axis to the point of measurement of the strain. The maximally strained components of the wire exist on the surfaces of the wire, or where $z = r$ in the case of a wire of uniform circular cross section.

For a homogeneous, isotropic beam, this definition can be extrapolated geometrically to describe the strain on a beam experiencing pure bending. With Figure 2.10 as a

reference image,

$$\epsilon = \frac{L - L_o}{L_o} = \frac{\theta(r_c + z) - \theta(r_c)}{\theta r_c} = \frac{z}{r_c}. \quad (2.24)$$

From this it is possible to estimate the maximum bending strain experienced by a

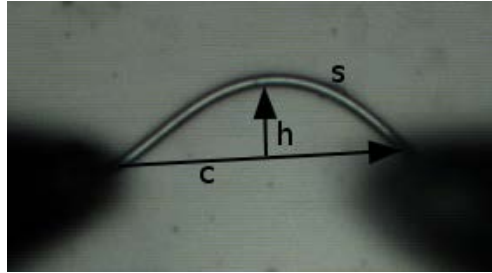


FIGURE 2.11: Scaled measurement parameters on microwire under applied stress.

deformed microwire. Using properly-scaled real-time images of the microwires under applied bending stress (as shown in Figure 2.11), the radius of curvature is found to be

$$r_c = \frac{c^2}{8h} + \frac{h}{2}$$

and therefore the strain

$$\epsilon = (z) \left(\frac{c^2}{8h} + \frac{h}{2} \right)^{-1}. \quad (2.25)$$

The maximum strain experienced by the wire is then

$$\pm \epsilon_{max} = \pm (r) \left(\frac{c^2}{8h} + \frac{h}{2} \right)^{-1}, \quad (2.26)$$

where $+\epsilon$ corresponds to tensile strain and $-\epsilon$ to compressive strain.

When considering piezoresistive effects, a notable characteristic of a wire strained with

bend deformation is the presence of both compressive and tensile strains within the wire. The neutral axis serves as a boundary distinction between the tensile-strained portion of the wire and the compressive-strained portion. A material of a given dopant type (n or p) will react electrically to tensile and compressive strain in an opposite manner, but not necessarily in proportion; for example, n-Si will exhibit negative piezoresistivity while undergoing tensile strain, and positive piezoresistivity while undergoing compressive strain [18], but the negative and positive responses may not be proportional in their sensitivity to the applied strain [42]. In a perfectly uniform wire the strain gradients should be equivalent on either side of the neutral axis [41], or $|\epsilon_{max}| = |\epsilon_{min}|$. While the beam bending model is developed predominantly for macroscopic situations [41], uniform strain gradients were observed at the microscale for ZnO microwires subjected to bend deformation in [43]. Photoluminescence spectra recorded at different locations about the neutral axis confirmed the symmetry of compressive and tensile strains in uniform microwires. This supports the use of the pure bending model on microwires at these length scales.

Under the assumption that the applied bending strain is pure and uniform, the tensile effects of the applied strain are argued to be the predominant contributors to the piezoresistive coefficient in n-type silicon [19, 42]. This is due, again, to charge transfer under crystalline deformation; tensile strain will cause a transfer of carriers from two longitudinal valleys to the four transverse valleys, resulting in a stronger ratio discrepancy of light carriers to heavy carriers under this mechanism than for the opposite response under compressive strain [30].

2.4 Doping Concentration Effects

As mentioned earlier, silicon intended for use in electronics is often doped with an impurity, such as boron (p-type) or phosphorus (n-type), in order to increase the amount of carriers in its lattice, thereby increasing its conductivity [44]. Notably, p-type doped and n-type doped silicon have opposite-sign gauge factors, negative and positive respectively [18, 45]. A negative gauge factor indicates that as applied compressive strain increases, the material's resistivity will decrease; a positive gauge factor means that as applied compressive strain increases, the resistivity increases as well. The doping concentration can be controlled to achieve the desired level of conductivity for a given sample of silicon. Degenerately or highly doped silicon will have a doping concentration in excess of 10^{18} carriers per cm^3 . While this high doping level significantly increases the conductivity of silicon, it can also have an effect on silicon's piezoresistive characteristics.

Generally, the piezoresistive response reduces as doping level is increased [46, 47]. This is postulated to be due to increased carrier interaction with dopant impurities in the lattice, reducing carrier mobility, as the doping concentration is increased. One study [48] noted anomalous behaviour for n-type silicon doped with phosphorus. The piezoresistive coefficient for the highly doped silicon showed a significantly increased response as the doping concentration neared 10^{20} cm^{-3} . Tufte [48] argued that this effect may be caused by high electron concentration raising the Fermi level of the silicon to the conduction band level, dramatically increasing conductivity.

2.5 Scaling and Growth Effects

In their 2006 study, He and Yang looked at the piezoresistive response of silicon nanowires experiencing tensile and compressive stresses. The wires investigated in the study were boron-doped, p-type crystalline silicon nanowires. It was shown that the wires' resistivity decreased when undergoing compressive stress, and increased when experiencing tensile stress [19], which is an example of the positive piezoresistive response expected for p-type silicon. The noted effect was stronger than that of bulk silicon, suggesting that significantly reducing the dimensions of doped silicon wires can increase their piezoresistive response. However, while [19] suggests that wires on the nano- and micro-scale should exhibit stronger resistivity change in response to strain, the study done in [20] shows that this effect may not in fact be due to an increased piezoresistance response, but is instead a result of charge trapping on the wires' surface. By modeling the resistivity change over time, they showed that the response is independent of strain, indicating that the giant piezoresistance proposed in [19] is not, in fact, a piezoresistive effect, but caused by hole and electron surface trapping. This would suggest that the piezoresistance coefficient for silicon nano- and micro-wires is not significantly different than that of bulk silicon.

Piezoresistive investigation of silicon has been predominantly focused on bulk and top-down silicon structures. Top-down refers to those structures (typically nano- or micro-wires or rods) that have been formed using an etching procedure. A silicon wafer is masked with dioxide and lithographically patterned. Then an etchant is used to remove

the filler silicon beneath the unmasked areas. The mask is then stripped, leaving behind high aspect ratio silicon structures [49]. This is a common method for microfabrication of silicon nano and microwires. In comparison, the bottom-up microwires investigated in this study are grown from a planar silicon surface by a chemical vapour deposition (CVD) vapour-liquid-solid process, which is described in more detail in Chapter 3. The resulting microwire structures have faceted surfaces and contain very few defects [50, 51], which results in higher fracture stresses and greater bending potential before failure [52]. Studies on the piezoresistivity of bottom-up structures have shown some anomalous effects; notably, a study performed on p-type bottom-up nanowires showed a reversal in the sign of the nanowires' piezoresistive response at high applied strains [53]. At these high strains (in excess of 3.5%), the piezoresistive coefficient of the wires reversed in sign, so that wires exhibited the characteristics of n-type wires instead of p-type. The authors suggested that this effect may be due to high hole mobility at high strains caused by the relatively defect-free structure of the bottom-up nanowires. This may indicate a cause for variation in the piezoresistive response for bottom-up structures as opposed to top-down or bulk structures; at the very least, it appears to indicate the relative purity and robustness of bottom-up structures makes them excellent candidates for piezoresistive investigation at high strains.

2.6 Surface Functionalization

Surface functionalization refers to the attachment of chemical functional groups to the surface of the silicon microwires. Surface functionalizations are predominantly performed to reduce native oxide growth on the surface of the silicon microwires. The functionalizations help to slow the growth of native oxide on the surface [54]. Oxide layers can impede light absorption in silicon and are therefore undesirable in the wider context of the project. The microwires investigated in this study were received with functional groups in place. The wires were surface terminated with thienyl groups. A selection of the samples were also backfilled with methyl groups. These surface modifications were not expected to have a significant effect on the piezoresistive characteristics of the microwires.

In [19], the piezoresistance coefficient was investigated for wires as-grown (indicating the presence of an oxide layer); wires treated with hydrofluoric acid (HF), which strips the native oxide layer and terminates the surface with hydrogen to prevent oxide growth; and wires treated with HF and then HNO_3 to create an artificial, controllable oxide layer. It was shown that the artificially oxidized wires showed a decreased piezoresistance response, while the H-terminated wires showed an increased piezoresistance response when compared to the as-grown wires. The sensitivity of the piezoresistive response to the surface states indicates that surface effects may play a role in the response of silicon's resistivity to changing strain. Both of these functionalizations performed (thienyl termination, methyl backfill) on the wires studied should equally retard the growth of native

oxide, so the piezoresistive response of the microwires should not be significantly affected by the presence of the thienyl and methyl groups. Recent research has shown that methyl termination of their surfaces have little effect on the electrical properties of silicon microwires [55].

2.7 Hypothesis

Based on established theory and recent literature, strong piezoresistive behaviour should be evident for the n-type silicon microwires investigated in this study. Degenerately doped wires should show reduced piezoresistive response when compared to wires with lower doping concentration. The surface functionalizations performed to reduce oxidation should not have a significant effect on the piezoresistive response of the microwires. Considering the dimensions of the wires in question (on the micron scale), it is not expected to see a large deviation in piezoresistive response when compared to bulk silicon. The mechanism of wire growth (CVD VLS bottom-up growth) may have an effect on the observed PR response, and any deviation from the expected PR response for bulk and top-down fabricated microwires is of certain interest from a scientific standpoint.

Chapter 3

Method

3.1 Sample Preparation

This study was undertaken on a variety of doped, surface-functionalized silicon microwires. The silicon wires used for testing were fabricated at the California Institute of Technology and sent to the University of Manitoba for characterization [56, 57]. The microwires were grown using a CVD (Chemical Vapour Deposition) process. The wires were grown on a doped (111) silicon wafer using patterned copper catalysts to produce uniform, (111) silicon microwires with a diameter of about 1.5 microns [57]. The mechanism of growth used was VLS (Vapour-Liquid-Solid) growth, in which a metal (in this case, copper) is used as a catalyst, speeding up a growth process which would normally rely on the very slow adsorption of silicon gas molecules on a solid silicon substrate. In

the VLS process, a vapour containing silicon, such as $\text{SiCl}_4:\text{H}_2$, is passed through a chamber containing a silicon substrate patterned evenly with liquid-alloy metal droplets via a photolithographic technique. The patterning makes use of silicon oxide to render the areas not patterned with metal catalyst inactive during the growth process. This ensures the patterned growth of high-fidelity microwires only in the areas where metal has been deposited. The SiCl_4 adsorbs to the metal droplets and diffuses towards the liquid-solid (for instance, Cu-Si) interface with the substrate, at which point nucleation occurs and silicon crystal growth begins. A metal silicide is formed at the interface of the catalyzing droplet and the silicon surface, therefore operating temperature must be in excess of the eutectic point of the metal catalyst and silicon. This mechanism is very useful to facilitate growth of uniform, regularly patterned micro- and nano-wires. Figure 3.1 shows an SEM image of an array of VLS-grown microwires from [56]. Once the growth process is

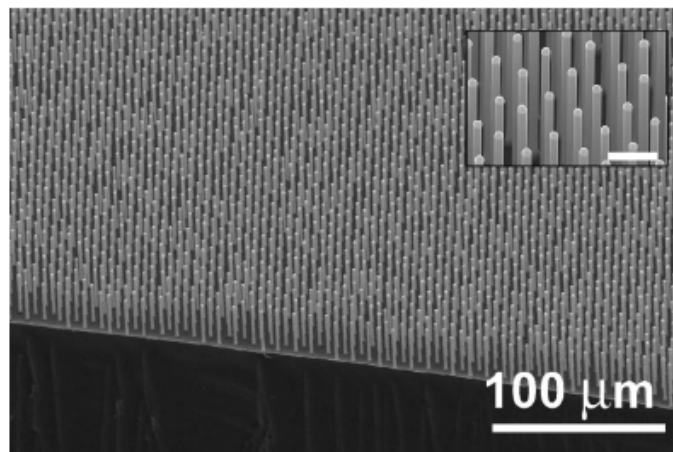


FIGURE 3.1: Silicon microwires grown by VLS chemical vapour deposition. Inset scale bar $10\mu\text{m}$. Used with permission. Copyright 2007, AIP Publishing LLC.

completed, the substrate can be removed from the CVD growth chamber.

The pre-grown microwires were received still on their growth substrate. The wires were received following surface functionalization with a variety of organic groups, including thiophene and methyl groups, to mitigate the growth of native oxide on the microwire surface [54]. In order to examine them individually, the microwire growth substrate was held above a vial containing HPLC-grade acetonitrile solution and the densely grown microwires were scraped from the substrate into the solution using a fine razor blade. Once the scrapings containing the microwires were suspended in the acetonitrile solution, the solution was agitated in a sonicator for thirty seconds in order to optimize the dispersion of the microwires in solution. Immediately thereafter the acetonitrile/microwire solution was deposited via pipette onto glass microscope slides in three 10 μl increments. The acetonitrile evaporated quickly, leaving the microwires suspended on the glass slide, as shown in Figure 3.2. The wires were then investigated in groups and individually under a microscope. Typically about 50 microwires were contained in one 10 μl deposition. The wires ranged in length from 10 μm to 100 μm . Each wire had an approximate diameter of 1.5 μm . The diameter of the microwires is controlled by the size of the metal catalyst droplet during the CVD growth process [56]. All of the images of the microwires used for illustration and analysis were captured using an Infinity 2 camera above a PSM-1000 microscope, and analyzed with the corresponding Lumenera Infinity Analyze software.

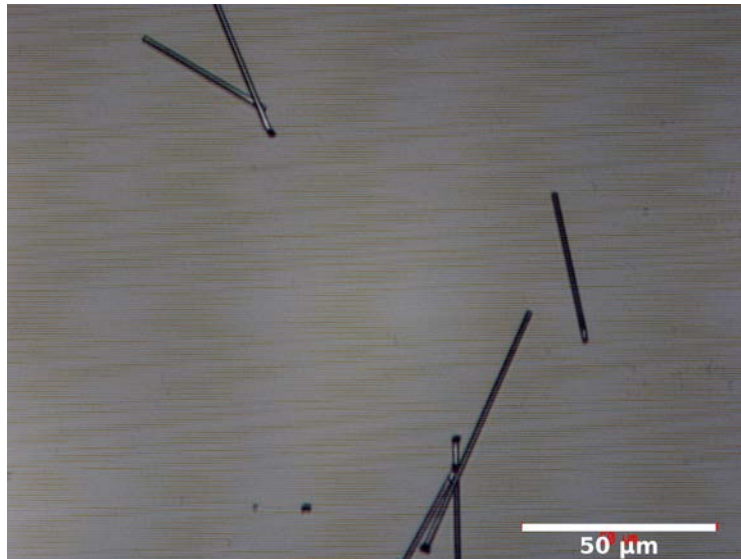


FIGURE 3.2: Silicon microwires deposited on a glass slide. Lengths varied due to position on growth substrate as well as breakage during removal procedure.

3.2 Electrical Testing

In order to test the electrical characteristics of the microwires, the microscope slide containing the microwires in solution was examined in a probing station (Süss MicroTec, Semiprobe) under a microscope (PSM-1000, Semiprobe). The slide was secured on a vacuum chuck to reduce vibrational interference. The individual wires were clearly identifiable at 100x magnification, and were typically analyzed under 400x magnification. In order to make electrical contact to the individual wires, two conductive tungsten (W) probes were brought into contact on either end of an individual microwire (see Figure 3.3). The probe holders used were of two types: conventional, manual probe holders (Semiprobe MA8000, Süss MicroTec PH100) and remotely controlled, piezoelectrically-driven robotic units (Imina Technologies Micromanipulator miBot BT-11). The probe tips used have a tip radius of 1 - 2 μm , a .14 - .16" taper, and are 1.25" long (American

Probe and Technologies model 72T-G3). The probing station was directly connected to

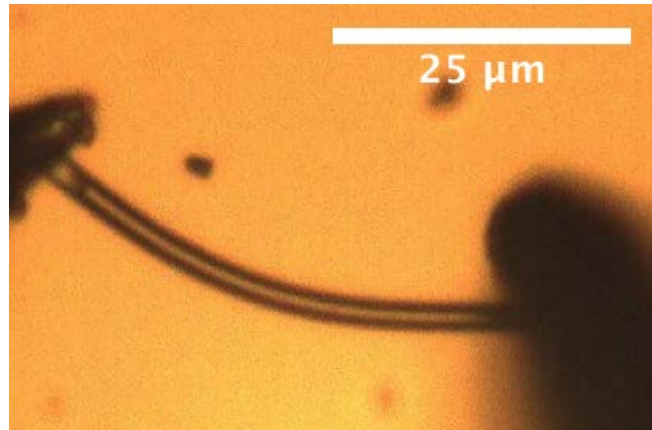


FIGURE 3.3: Tungsten (W) probes brought into direct contact with a single silicon microwire.

an Agilent 4155C semiconductor parameter analyzer, and the software used to extract and analyze the electrical response of the wires was Agilent EasyExpert.

Two experiments were performed. First, a current-voltage measurement was performed by sweeping an applied voltage bias while two probes were in ohmic contact with a microwire. This bias was typically set for either a small bias regime of -60 mV to 60 mV or a larger bias of -200 mV - 200 mV. The small bias regime more closely mimicked eventual operating conditions, but was less stable instrumentally, whereas the larger bias regime produced consistently reproducible and comparable results. The probing station then returned the current response for each 2 mV bias interval. Figure 3.4 shows a schematic of the electrical circuit formed by this system. The second set of data required I-V/t measurements. A bias of 200 mV was set and the current response over time was plotted for a set time interval of 60 - 120 seconds. This temporal analysis helped to quantify any instrumental drift or relaxation of the applied probe pressure over time. Both of these

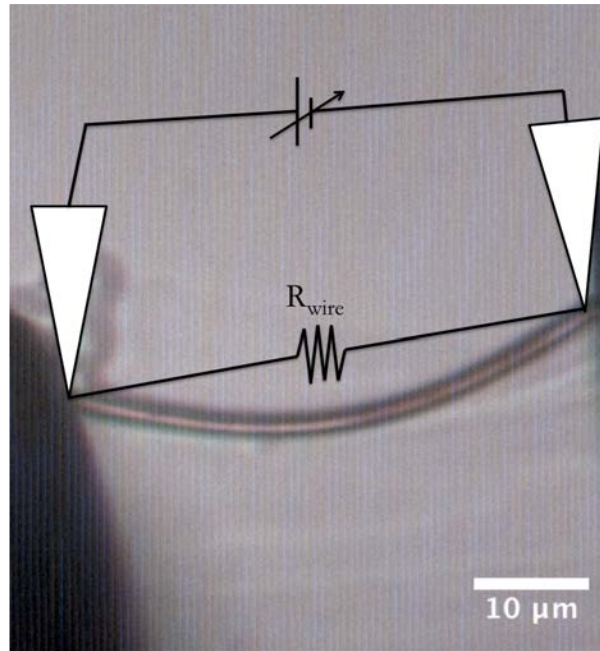


FIGURE 3.4: Electrical circuit formed by tungsten probe - silicon wire - tungsten probe system.

measurements required that the tungsten probes make consistent ohmic contact to the microwires.

3.2.1 Making Ohmic Contact

The individual silicon microwires were not anchored on either end by a conductive pad or contact to facilitate electrical contact. In order to make ohmic contact to the silicon microwires, local mechanical pressure was directly applied using the tungsten probes. An applied pressure of $11 \text{ mN}/\mu\text{m}^2$ on single crystalline silicon will achieve ohmic contact directly beneath the conductive contact. This effect is facilitated by a phase change in silicon, causing it to behave, in the vicinity of the applied pressure, as a metal rather than a semiconductor [17, 58]. This effect was more rigorously discussed in Chapter 2 of

this thesis.

Soft contact to the silicon wires will produce a rectifying or Schottky contact. Further applied pressure is necessary to make the transition from a Schottky contact to an ohmic contact. In order to quantify how much pressure is necessary, the probe and probe holder systems were analyzed using a fine balance. The height of the probes is controlled by a dial on the probe holders, referred to from now on as the vertical control dial. To investigate the pressure applied by an incremental turn of the vertical control dial, a probe was slowly lowered and brought into contact with a fine balance. When the probe achieved soft contact with the balance plate, the balance was zeroed. The vertical control dial was marked at this position to indicate the starting position of the dial. From that point on, each successive turn of the vertical control dial produced a corresponding response on the balance, proportional to the force applied by the probe. This response was recorded for every 1/8 turn of the vertical control dial until the point of saturation, wherein additional turns of the control dial produced no further change on the balance's reading. The balance reading for each 1/8 turn was given in mass units, and using this data as well as the dimensional parameters of the probes, it is possible to determine the pressure applied by the probes when the vertical control dial is turned 1/8 of a full rotation. The pressure was calculated using the definition

$$P = \frac{F}{A}, \quad (3.1)$$

where F is the applied force (N) and A is the contact area (m^2). This equation can be further expanded to give

$$P = \frac{mg}{\pi r^2}, \quad (3.2)$$

where $g = 9.80665 \text{ ms}^{-2}$, the gravitational acceleration, and m , in this case, is the mass response as recorded by the balance, in kg.

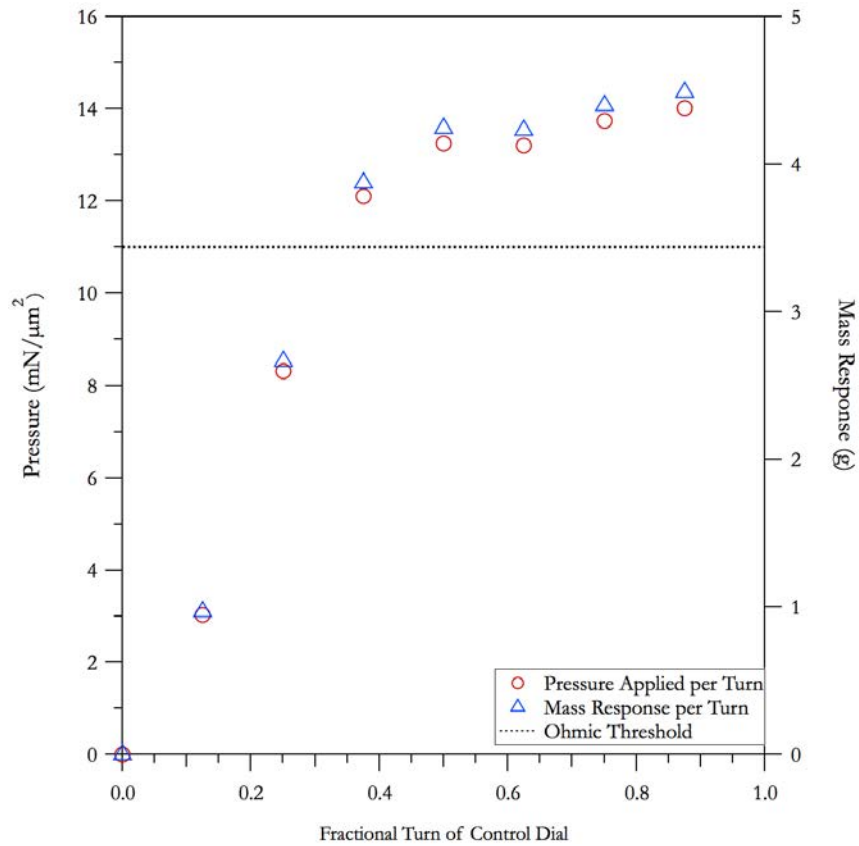


FIGURE 3.5: Applied pressure as a function of incremental turns of the probe holder control dial. The horizontal line represents the threshold of $11 \text{ mN}/\mu\text{m}^2$ which is required to make direct ohmic contact to single crystalline silicon.

The area of contact was determined using r , defined as the radius of the tungsten probe tip in contact with the balance, which in this case was $1\mu\text{m}$. Figure 3.5 shows the change

in applied pressure corresponding to successive turns of the control dial on the probe holder. From this it is possible to determine that a consistent pressure in excess of the minimum $11 \text{ mN}/\mu\text{m}^2$ is achieved by turning the control dial at least $3/8$ of a turn further downward from the point of soft contact as indicated by the starting position. Past a

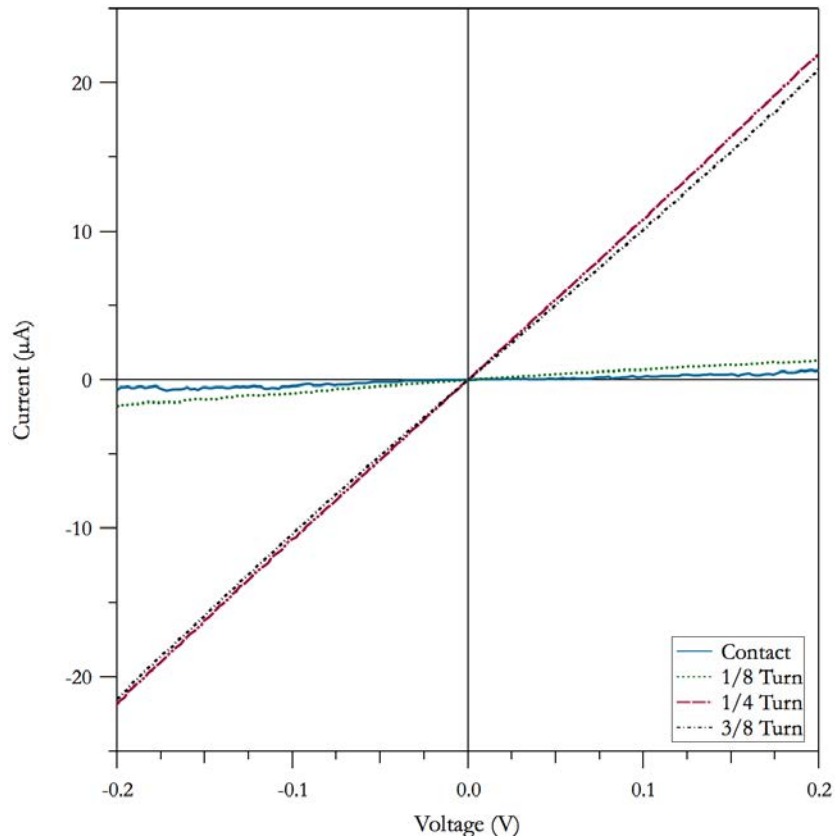


FIGURE 3.6: Current-voltage curves for incremental downward turns of the probe control dial, showing strong ohmic behaviour after 1/4 turn.

$3/4$ turn of the control dial, the system reached a saturation point and no further significant downward pressure was achieved through successive turns. Figure 3.6 shows the IV curves for dial turns corresponding to soft contact, $1/8$ turn, $1/4$ turn and $3/8$ turn. It illustrates strong and consistent ohmic contact achieved at $1/4$ turn and maintained through $3/8$ turn. Prior to that the contact was rectifying.

Further analysis showed that there is some reduction in applied probe pressure over time when using the manual probe holders, most likely due to relaxation of the spring controlling the manipulator. This was found to stabilize within a minute of applying downward pressure.

3.2.2 Determining Doping Concentration

The doping concentration was calculated in order to determine its effect on the gauge factor, using a method modified from [17]. First, a series of successive I-V curves was taken, with one tungsten probe held stationary on one end of the microwire, and the other tungsten probe discretely stepped towards the first (see Figure 3.7). At each separation distance, a new I-V curve was taken and the resistance extracted. In doing this, it was possible to plot the measured resistance versus separation distance for each microwire. The slope of the plots shown in Figures 4.4 and 4.5 will be in units of $\text{k}\Omega/\text{cm}$. In order to extract the resistivity from this information, the relationship

$$\rho = \frac{(R)(A)}{\ell}$$

is employed, where R is the resistance, ℓ the length (or separation distance between the two active measuring probes) and A the cross-sectional area of the wire. Therefore the slope of the resistance versus separation plot can be substituted for $\frac{R}{\ell}$ and the resistivity for the wire determined.

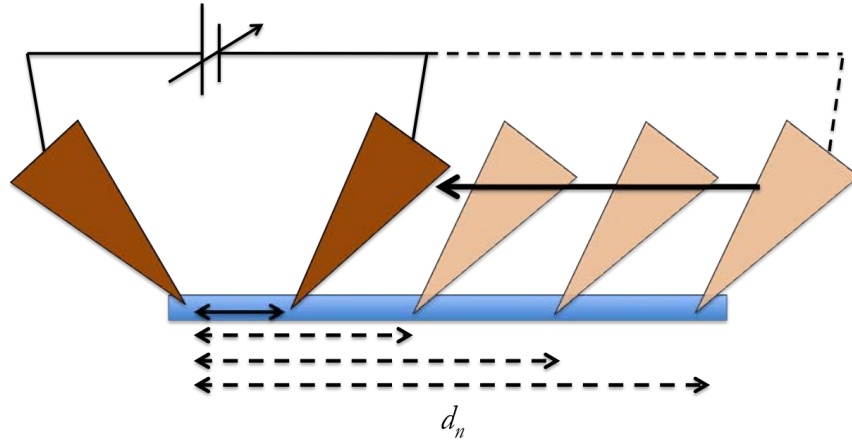


FIGURE 3.7: The separation distance d_n between the two active tungsten probes was decreased in intervals, with a resistance measurement performed at each stop, for n intervals along the length of a microwire.

The doping concentration can be determined using the mobility-dependent definition of the resistivity,

$$\rho = \frac{1}{(n_e)(\mu)(q)}, \quad (2.14 \text{ revisited})$$

where μ is the electron mobility, which in silicon is $1414 \text{ cm}^2\text{V}^{-1}\text{s}^{-1}$; q is the charge of the electron, $1.602 \times 10^{-19} \text{ C}$, and n_e is the concentration of carriers (in the case of n-Si, electrons). Rearranging, the doping concentration of the wire in question can be determined from

$$n_e = \frac{1}{(\rho)(\mu)(q)}.$$

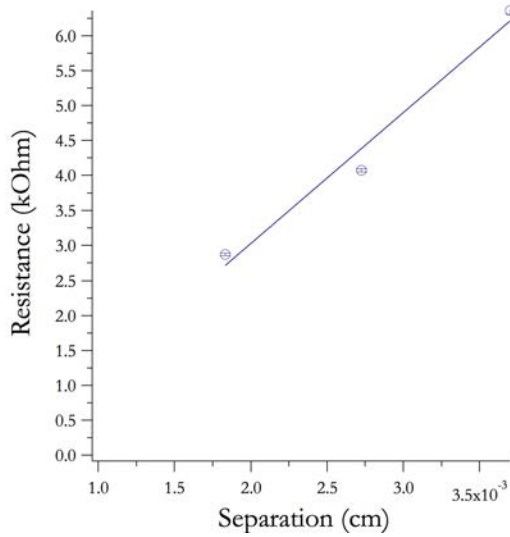


FIGURE 3.8: Resistance versus separation distance for the first sample, indicating a doping concentration of $(1.7 \pm 0.1) \times 10^{17} \text{ cm}^{-3}$

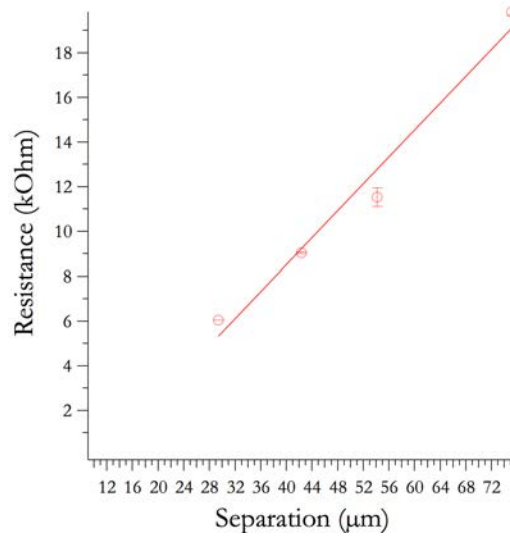


FIGURE 3.9: Resistance versus separation distance for the second sample, indicating a doping concentration of $(3.6 \pm 0.1) \times 10^{17} \text{ cm}^{-3}$

3.2.3 Effect of Probe Oxidation on Quality of Probe-Silicon Contact

Tungsten oxidizes at room temperature; however the growth of native oxide is slow, on the order of 10\AA for 1 hour of oxidation in a pure oxygen environment at 23°C [59]. The effect of oxidized tungsten probes on the validity of the microwire conductivity tests was investigated. Unetched tungsten probes were used to measure the current response across a uniform FTO plate with two sputtered silver (Ag) contacts 0.9 cm apart. This was repeated three times, with the probes brought completely out of contact with the FTO plate surface between each measurement. The resistance can be extracted from an I-V sweep using the relation

$$V = IR, \quad (3.3)$$

where V is the applied bias voltage and I is the corresponding current response. In the case of an ohmic or linear response, the line equation can be rewritten as

$$I = \frac{1}{R}V \quad (3.4)$$

where the slope of the curve gives the inverse of the resistance. From this relationship the resistance for each I-V sweep was determined and recorded.

Following these measurements, the tungsten probe tips were immersed in 2M KOH solution for 30 seconds to facilitate etching. They were then rinsed with DI water and dried using a dustless lab wipe. Immediately thereafter, the electrical test was repeated using the same method. One day later, the process was repeated again. Figure 3.10 shows the averaged I-V curves for each trial. The average resistances for each measurement are tabulated in Table 3.1. The measurements suggest that the tungsten probes do not grow a native oxide in room temperature which is significantly thick enough to affect the system resistance reading within the limits of error.

	Resistance (Ω)
Prior to Etching	20 ± 1
Five Minutes After Etching	20 ± 2
One Day After Etching	23 ± 1

TABLE 3.1: Resistance values for uniformly-separated tungsten probes on silver contacts sputtered on an FTO plate prior to etching with KOH, five minutes after etching, and one day after etching.

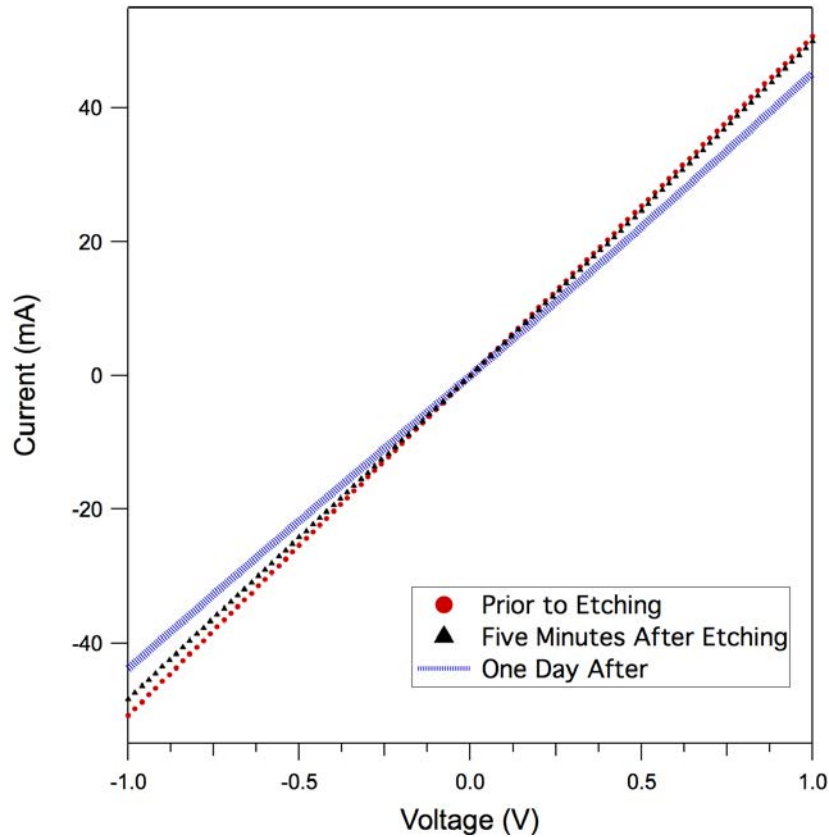


FIGURE 3.10: Current-voltage curves for tungsten W probes on FTO substrate prior to etching with KOH, immediately after etching, and a day after etching.

3.2.4 Effect of Illumination

The effect of analyzing the wires under the microscope light versus in darkness was investigated. The wires were isolated from light in a UV-blocking box around the probing station. The light control dial was located outside of the box, so that the microscope light could be turned on and off without the need to open and close the light-shielding door. In order to determine whether illumination had an effect on the current response of the wires, the current response was recorded for ten seconds first with the light off, and then this trial was repeated with the light on. The resulting current response can be seen in Figure 3.11. There is no difference in the current response under illumination versus in darkness

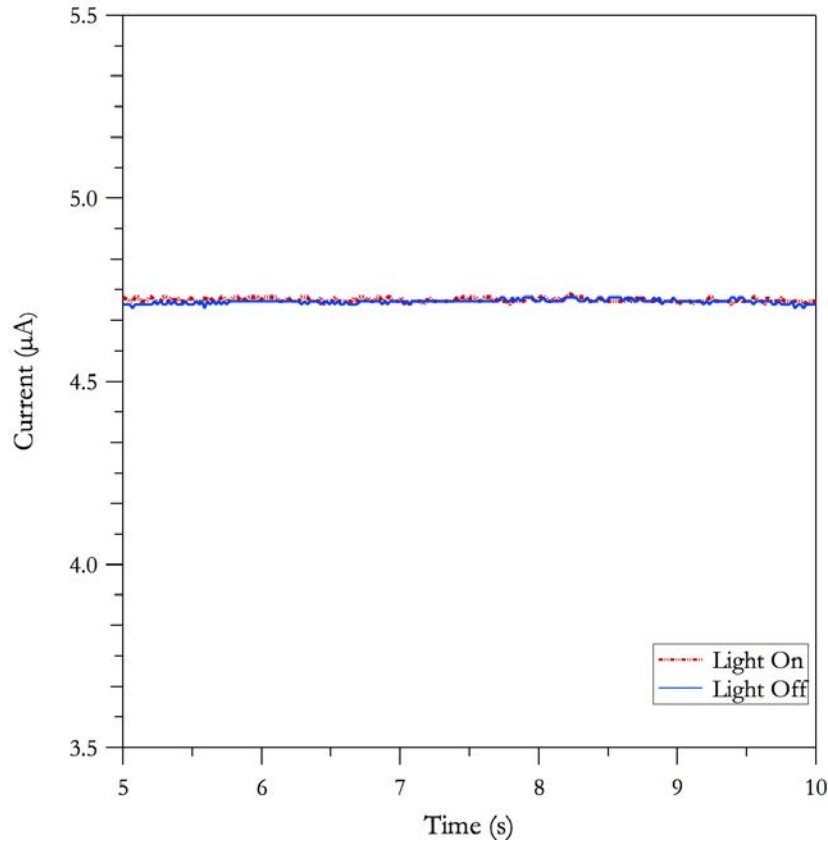


FIGURE 3.11: The effect on current response of silicon microwires under illumination (light on) and in darkness (light off).

within $0.1 \mu\text{A}$. Microwires with lengths of $\sim 100\mu\text{m}$ should generate a photocurrent of approximately 20 nA under one-sun conditions [60]. As the current observed along the length of the wire under an applied bias of 200 mV is three orders of magnitude greater than this, the difference in response is not significant for a wire investigated in the dark versus under illumination for this study. This trial was performed in order to confirm that the piezoresistive responses of the microwires should not change if the measurements were captured under the low-frequency illumination of the microscope light, or in complete darkness within the UV-blocking box. However, for consistency all experimental trials were performed with the microwires exposed to incident light from the microscope.

3.3 Strain Application

Once ohmic contact was successfully made to the microwires, the wires could be mechanically strained, and their electrical response to increasing bend deformation determined. Mechanical strain was applied using the tungsten probe manipulators. The manipulators have three dimensional control dials. The up/down control was used to apply the downward pressure necessary for ohmic contact, as detailed previously. There is also an x-direction and a y-direction control within the plane of the microscope slide. One probe was held fixed as the other was moved towards the first using the x- and y- control dials. This caused the microwire held between them to bend under the increasing strain. This method is illustrated in Figure 3.12. This process was repeated for different applied forces

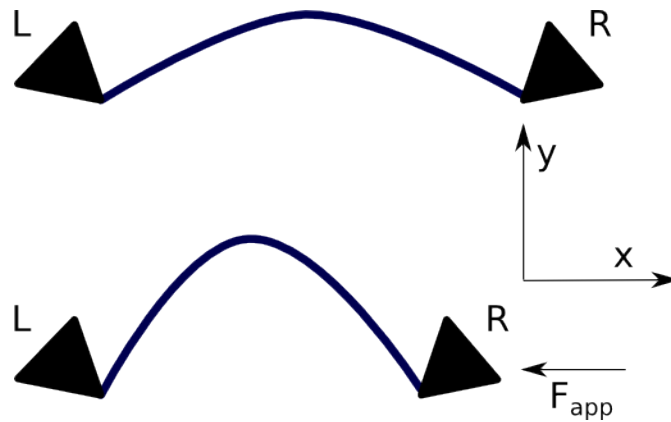


FIGURE 3.12: Application of mechanical strain to microwires. The left probe is held in a fixed position and the right probe is moved incrementally towards it using the x-direction control dial on the probe manipulator. The silicon wire experiences strain and this induces a bend deformation in the wire.

(and therefore different corresponding bend deformations) until the point of microwire

failure, when the wire would snap and break the electric circuit. While the x- and y- controls were moved to facilitate the change in strain, the up-down controls were unchanged to minimize changes in the tungsten probe-silicon wire contact.

3.3.1 Ex-Situ Quantitative Analysis

In order to quantify the amount of strain applied to the microwire under analysis, a dimensional calculation was undertaken using the definition of maximum tensile strain

$$\epsilon = \frac{z}{\frac{c^2}{8h} + \frac{h}{2}} \quad (2.25 \text{ revisited})$$

as was derived in Chapter 2. The parameters c and h can be extracted from a properly scaled microscope image as shown previously in Figure 2.11. The images were obtained under 400x magnification using a PSM-1000 microscope and were analyzed using ImageJ software.

Chapter 4

Results and Discussion

4.1 n-Si Microwires

4.1.1 Set A

A selection of (111) n-type silicon wires were tested which had been previously terminated with thienyl and backfilled with methyl groups. These wires were typically between 40 - 70 μm in length, and had a doping concentration of $(1.7 \pm 0.1) \times 10^{17} \text{ cm}^{-3}$ as determined by the experimental method outlined in the previous section as an average across a selection of the set.

The current response for a wire strained was consistently and markedly greater than that

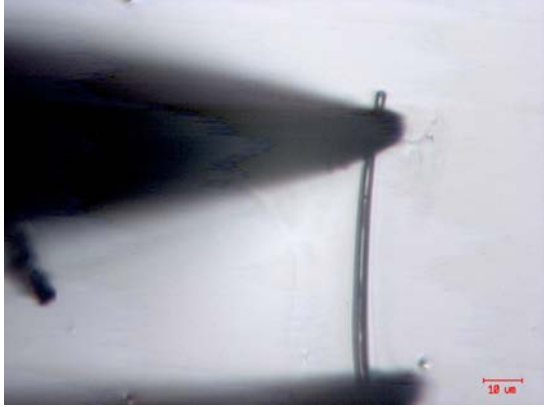


FIGURE 4.1: Under no applied strain.

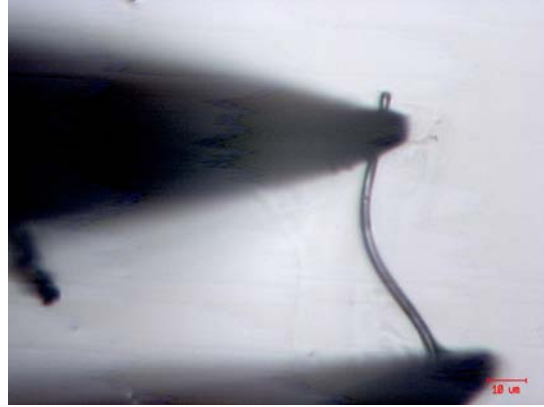


FIGURE 4.2: Under an applied bending strain of 2.9%.

for a wire unstrained, indicating a lower resistivity in the strained wires, as illustrated in Figure 4.3.

The gauge factors for 6 microwires from set A are shown in Table 4.1. The average gauge factor is calculated to be -6 ± 2 . Taking into account the Young's modulus Y for single-crystalline (111) silicon, 188 GPa, it is possible to calculate the average longitudinal piezoresistive coefficient, Π , for this sample:

$$\begin{aligned}\Pi &= \frac{GF}{Y} \\ \Pi &= \frac{(-6 \pm 2)}{188 \times 10^9} \\ \Pi &= (-3 \pm 1) \times 10^{-11} \text{ Pa}^{-1}\end{aligned}$$

This piezoresistive coefficient is within two orders of magnitude of that expected for n-type silicon of this dopant concentration, given in one study by $-102 \times 10^{-11} \text{ Pa}^{-1}$ [18]. However, significant variations in the piezoresistive coefficient of n-type silicon have been reported in different studies [30].

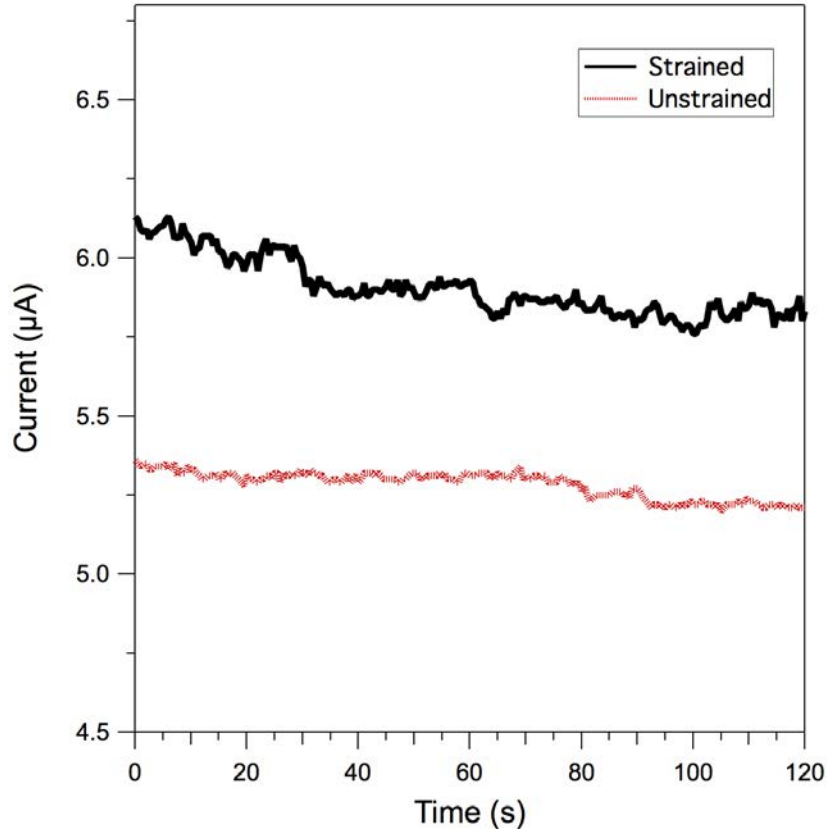


FIGURE 4.3: The current response of Sample 2 of the Set A concentration microwires, for both unstrained and strained (1.7%) trials at a set bias of 0.2 V.

Sample	Gauge Factor (unitless)	Error
1	-7	± 1
2	-8	± 1
3	-4	± 2
4	-4	± 1
5	-3	± 1
6	-9	± 1
Avg	-6	± 2

TABLE 4.1: Experimentally determined gauge factors for Set A.

4.1.2 Set B

Set B had a doping concentration of the same order as Set A but slightly higher, determined to be $(3.6 \pm 0.1) \times 10^{17} \text{ cm}^{-3}$ using the experimental method outlined in Section

3.2.2. The wires had also been previously functionalized with thienyl groups as in the case of set A, but were not backfilled with methyl. The wires had a typical length of 20 - 60 μm . The gauge factors for a set of 5 microwires are shown in Table 4.2. These

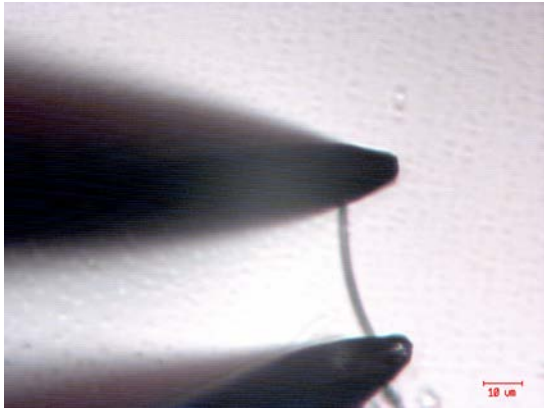


FIGURE 4.4: Sample 1 under no applied strain.

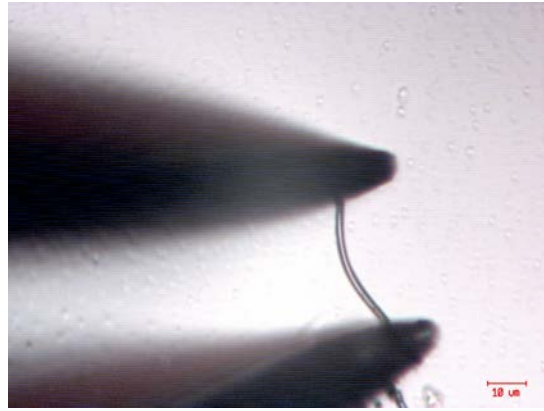


FIGURE 4.5: Under an applied bending strain of 2.4%.

values show an average over all trials performed, using both the iterative I-V method and the current response method as detailed in Section 3.2. Figure 4.6 shows the fractional change in resistivity as a function of applied strain for four of the wires of Set B, illustrating their consistent responses with an average slope of -14 ± 3 . This gives a value of the gauge factor for Set B using the iterative I-V method of data collection.

The average gauge factor is calculated to be -10 ± 3 , and as before the PR coefficient can be calculated using the Young's modulus,

$$\begin{aligned}\Pi &= \frac{GF}{Y} \\ \Pi &= \frac{(-10 \pm 3)}{188 \times 10^9} \\ \Pi &= (-5 \pm 2) \times 10^{-11} \text{Pa}^{-1}.\end{aligned}$$

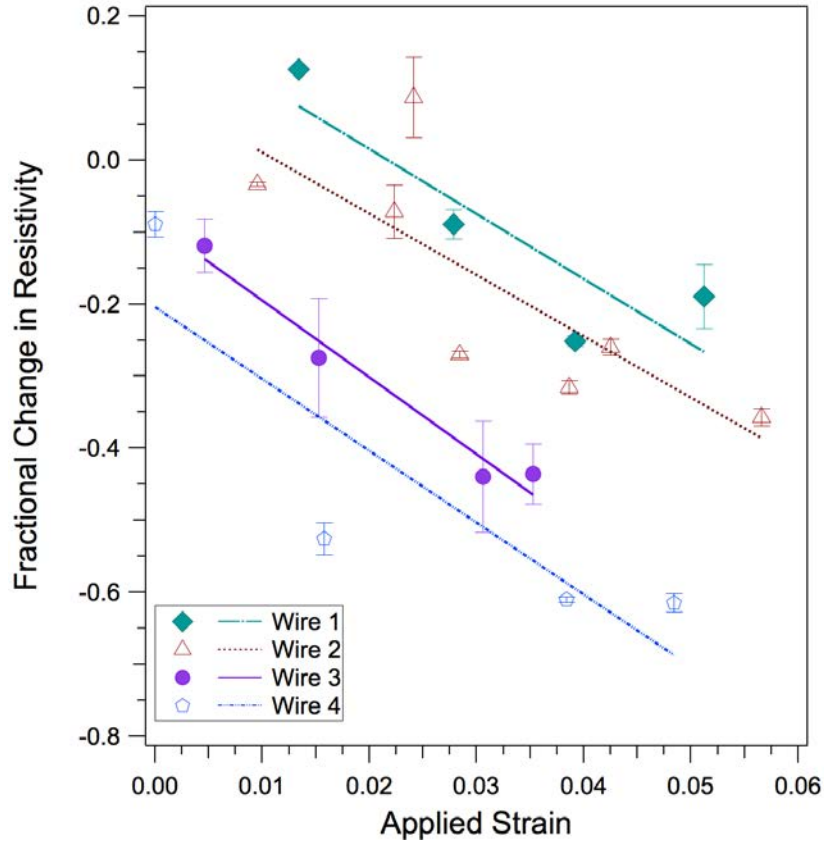


FIGURE 4.6: The fractional change in resistivity plotted as a function of strain for four individual wires in Set B, showing consistent trends with an average slope of -14 ± 3 , which corresponds to the gauge factor for this set.

This result indicates a stronger piezoresistive response for the increased doping concentration. This change in Π is likely due to the increase in dopant concentration, as the piezoresistive response has a strong dependency on the doping level, as discussed in Section 2. However, this result is in contention with the generally expected response of single-crystalline silicon, wherein increased doping concentration yields a reduced piezoresistive response [46–48].

Sample	Gauge Factor (unitless)	Error
1	-9	± 2
2	-8	± 3
3	-8	± 3
4	-12	± 2
5	-11	± 4
Avg	-10	± 3

TABLE 4.2: Experimentally determined gauge factors for thienyl-terminated, non-backfilled microwires with a doping concentration of $(3.6 \pm 0.1) \times 10^{17} \text{ cm}^{-3}$ (Set B).

4.1.3 Set C

The third set of microwires were doped to degenerate levels with a dopant concentration of $(6.8 \pm 0.8) \times 10^{20} \text{ cm}^{-3}$. The microwires had typical lengths of 60 - 100 μm . This set of degenerately doped microwires showed a very strong piezoresistive response. The gauge factors of a set of 5 microwires are tabulated in Table 4.3. Performing the same

Sample	Gauge Factor (unitless)	Error
1	-34	± 2
2	-46	± 2
3	-22	± 1
4	-24	± 2
5	-25	± 4
Avg	-30	± 9

TABLE 4.3: Experimentally determined gauge factors for thienyl-terminated, non-backfilled microwires with a doping concentration of $(6.8 \pm 0.8) \times 10^{20} \text{ cm}^{-3}$.

piezoresistive coefficient calculation that was used for the previous microwire sets, the degenerately doped set is shown to have a piezoresistive coefficient of $(-16 \pm 5) \times 10^{-11} \text{ Pa}^{-1}$, which is significantly higher than the responses recorded for either set in the 10^{17} cm^{-3} range. Figure 4.7 shows the electrical response of the degenerately doped wires as they respond to increasing strain.

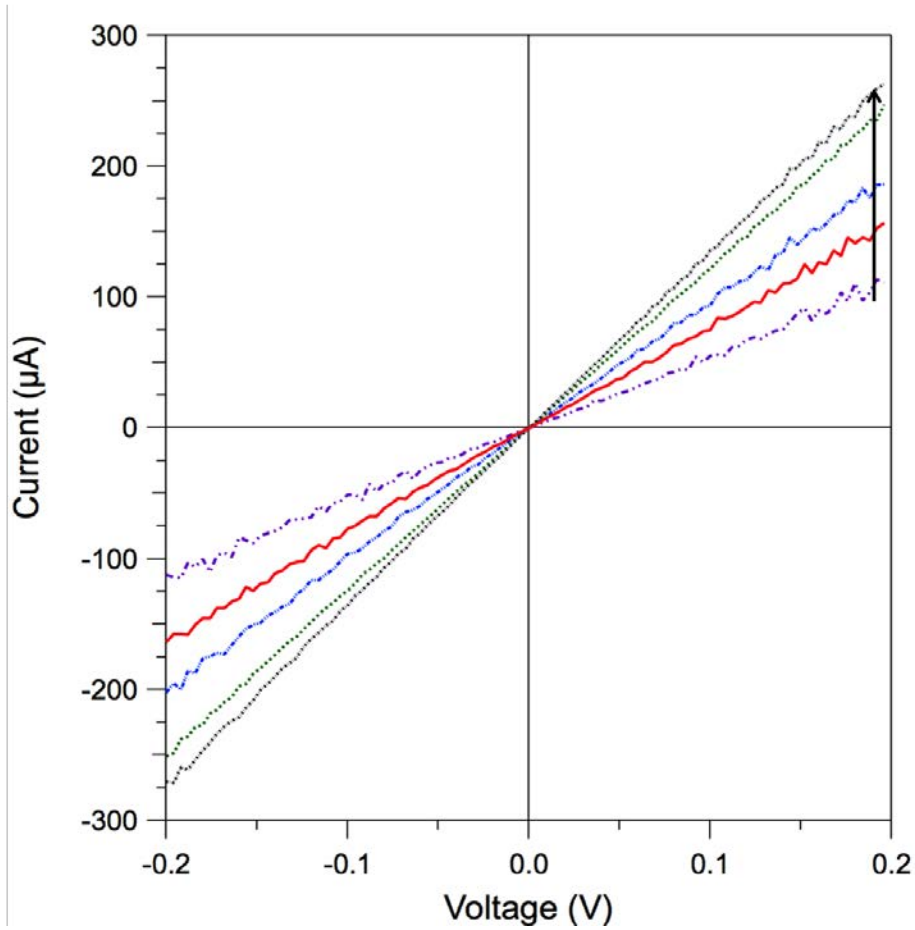


FIGURE 4.7: The electrical response of a degenerately doped microwire in response to strain. The arrow indicates the direction of increasing applied strain, from 0% to 2.2%.

4.1.4 Comparison

Results show a small difference between the two sets of bottom-up, (111) lower doped n-Si microwires, with Set A, having a doping concentration of $(1.7 \pm 0.1) \times 10^{17} \text{ cm}^{-3}$, giving a PR coefficient of $(-3 \pm 1) \times 10^{-11} \text{ Pa}^{-1}$, and Set B, with a nominally higher doping concentration of $(3.6 \pm 0.1) \times 10^{17} \text{ cm}^{-3}$, giving a PR coefficient of $(-5 \pm 2) \times 10^{-11} \text{ Pa}^{-1}$. The variation in doping concentration between sample sets A, B and C is the most likely source of the difference in piezoresistive coefficient observed. The most lowly doped samples exhibited the lowest piezoresistive response. A statistical t-test analysis was performed in

order to rule out the possibility of the two sets having the same gauge factor within experimental error. The t-test gave a p-value of 0.02, strongly supporting the presumption of different gauge factors for the two sets A and B. An analysis of the degenerately doped Set C ($(6.8 \pm 0.8) \times 10^{20} \text{ cm}^{-3}$) gave a piezoresistive coefficient significantly higher, with a value of $(-16 \pm 5) \times 10^{-11} \text{ Pa}^{-1}$. The results are tabulated in Table 4.4.

Set	Doping Conc. (cm^{-3})	Avg. Gauge Factor	PR Coefficient (10^{-11} Pa^{-1})
A	$(1.7 \pm 0.1) \times 10^{17}$	-6 ± 2	-3 ± 1
B	$(3.6 \pm 0.1) \times 10^{17}$	-10 ± 3	-5 ± 2
C	$(6.8 \pm 0.8) \times 10^{20}$	-30 ± 9	-16 ± 5

TABLE 4.4: Experimentally determined PR coefficient results for all sets

These results suggest that increasing the doping concentration of the microwires will correspondingly increase their piezoresistive response, which is contrary to most literature on bulk and top-down silicon structures [46–48]. Figure 4.8 shows the fractional change in resistivity as a function of strain for all three sets, where the slope of each linear fit gives the approximate gauge factor for each set. Set C has a more pronounced resistivity response to increasing strain. The cause of this anomalous increase in piezoresistive response for degenerately doped wires is unclear. While the piezoresistive values for each set are within an order of magnitude of those reported for bulk silicon [18, 48], it is the distinct trend of increasing piezoresistive response with increasing doping concentration that is unexpected. This may indicate that the anomalous behaviour is due to some mechanism of the bottom-up microwires that is not present in bulk or top-down silicon structures.

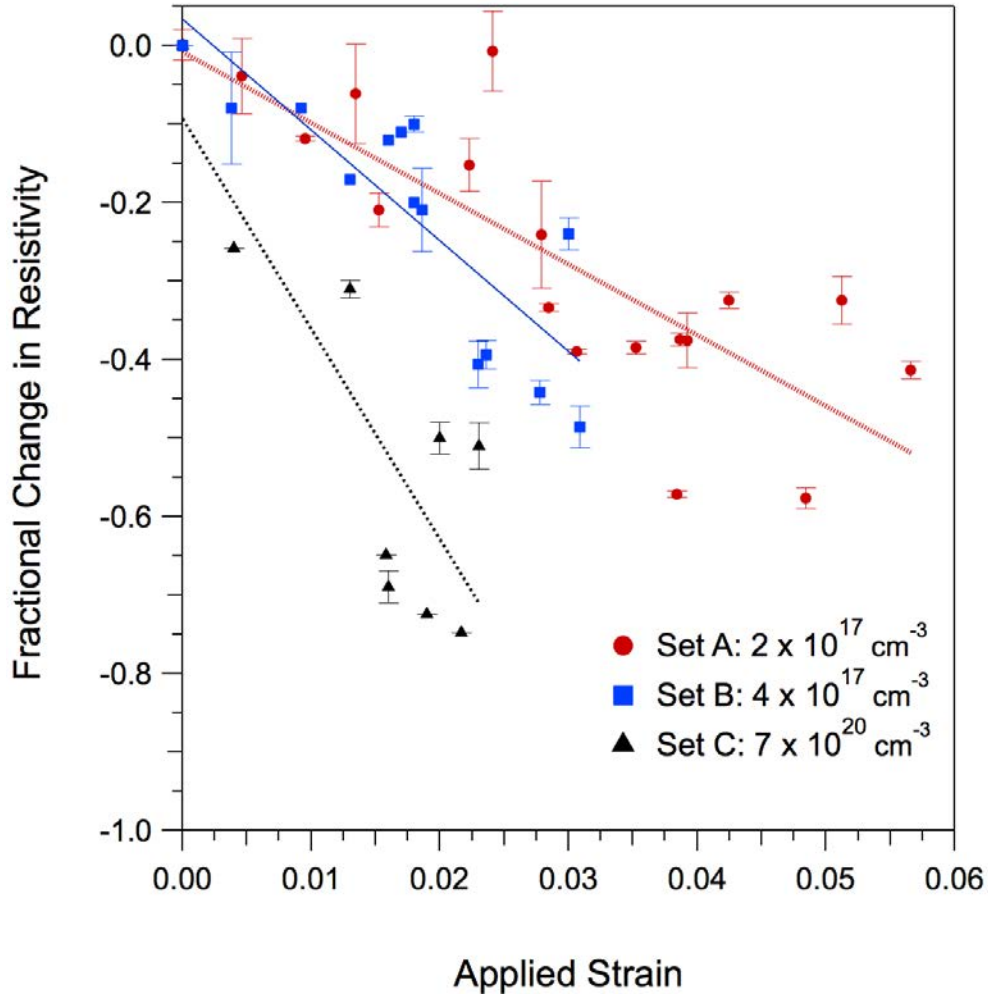


FIGURE 4.8: A direct comparison between the three sets of doped n-type microwires shows an appreciably stronger response for the more highly doped wires (Set C) than for either set of wires with doping concentration on the order of 10^{17} cm^{-3} (Sets A and B).

As discussed in Section 2.5, there has been limited piezoresistive testing performed on CVD-grown, bottom-up microwires [30], but they do exhibit two notable characteristics distinct from top-down microwires, those being faceted surfaces and the presence of metallic impurities resulting from their growth process [50, 56, 57] (in the case of the wires studied, the metallic impurity present would be copper). Copper impurities in the bulk of the microwire will introduce deep traps, scattering sites and recombination centers for

electrons [61–63]; however, this effect would be expected to reduce the mobility of carriers along the wire as opposed to increasing it. Additionally, the amount of copper contamination should be roughly the same for lower-doped and higher-doped wires [50, 56], so is not likely to be a valid explanation for the increased conductivity of degenerately doped, strained microwires. Surface faceting is also unlikely to have a significant contribution to wires on the microscale, as bulk effect should dominate at these dimensions [19].

As discussed in Section 2.5, a study performed on p-type bottom-up nanowires reported anomalous behaviour: when the p-type wires were subjected to high strains (in excess of 3.5%), their piezoresistive coefficient reversed in sign, essentially causing them to behave as n-type wires [53]. The authors argued that this unexpected resistivity decrease was due to a significant increase in hole mobility at high strains, facilitated by the relatively defect-free structure of the VLS-grown nanowires, which allowed for testing at high strain levels. Alternatively, the observed trend may be due to some other mechanism of the n-type microwires. In [48], author Tufte notes a similar response in degenerately doped bulk silicon (on the order of 10^{20} cm^{-3}), which he posits is due to the Fermi level of the silicon approaching the conduction band due to a very high concentration of electrons in the degenerately doped silicon.

4.2 Implications for the Solar Device

The n-type wires investigated in this study will comprise the anode component of the artificial photosynthesis device described in Chapter 1. A main goal in optimizing this device is to reduce system resistance in the anode-polymer-cathode system. As mentioned before, the system resistance is a series summation of the resistances illustrated in Figure 4.9.

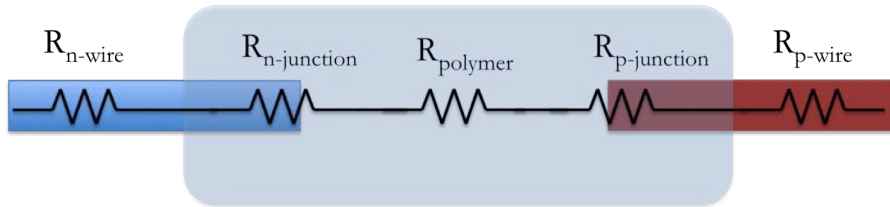


FIGURE 4.9: Schematic showing the series resistance components of the overall micro-wire/polymer system. A reduction in any of the five resistive components will result in a reduction in overall resistance.

This can be described by the equation

$$R_{system} = R_{n-wire} + R_{n-junction} + R_{polymer} + R_{p-junction} + R_{p-wire} \quad (4.1)$$

where $R_{n,p-junction}$ are the contact resistances of the n-wire/polymer and p-wire/polymer respectively, $R_{polymer}$ is the resistance of the conducting polymer membrane, and $R_{n,p-wire}$ are the resistances of the n-type and p-type embedded wires [64]. In the work performed by Yahyaie in 2011 it was shown that the predominant contribution to the system series resistance comes from the contact resistance. His model experimental system showed the values tabulated in Table 4.5 for an n-wire-polymer embedded system. In this work the

focus is on the n-wire/polymer system, referred to as $R_{n-system}$.

$R_{n-wire}(k\Omega)$	$R_{n-junction}(k\Omega)$	$R_{polymer}(k\Omega)$	$R_{n-system}(k\Omega)$
18	850	2	870

TABLE 4.5: Experimentally determined resistances for n-type wire/polymer prototype system.

While the contact resistance of the n-type wire/polymer junction is far and away the most significant contributor to the overall series resistance, the second most significant resistance comes from the resistance of the wire itself. Therefore, a step towards reducing n-system series resistance (and therefore reducing the voltage drop across the microwire/polymer interface) could involve reducing the resistivity of the n-type microwires. This study's investigations into the gauge factor of the n-Si microwires have illustrated the potential to lower the resistivity up to 41% for an applied bending strain of 5.7% for Set A microwires. This reduction in n-Si resistivity will help to lower the overall system resistance, if the required strain can be consistently applied to the microwires within the final device. However, continuous application of this strain level is difficult and may not feasibly be translated to pure tensile or compressive strain before failure, so a more reasonable value would be less than 2% strain. Percentage reductions in resistance for the three sets investigated can be seen in Table 4.6.

Set	Feasible Strain	Reduction	Max Strain	Max Reduction
A	1%	12±2%	5.7%	41±3%
B	1.3%	17±3%	3.1%	49±3%
C	1.5%	65±3%	2.2%	75±3%

TABLE 4.6: Feasible and maximum achieved reductions in resistivity for all three sets.

These values could feasibly provide a 17% decrease in resistance for the $100\mu\text{m}$, 10^{17}cm^{-3} n-type microwires explored by Yahyaie under a 1.3% applied strain, reducing $R_{n\text{-wire}}$ to $15\text{k}\Omega$. For a more extreme applied strain of 3.1%, it is possible to lower the resistance of the wires to $9\text{k}\Omega$, resulting in an overall reduction in n-system series resistance of 1%. This is indicative of the feasibility of applying piezoresistivity as a method to reduce the overall system resistance, although it is not significant when compared with the contribution of the junction resistance. It may be of more utility in the p-type wire/polymer system, where the contact resistance ($120\text{k}\Omega$) is less significant a contributor and the wire resistance itself ($50\text{k}\Omega$) is more significant when compared to the n-system.

Chapter 5

Conclusion

An integrated artificial photosynthesis device has been proposed to evolve hydrogen from sunlight and water, providing a clean, renewable and essentially limitless source of chemical fuel. A prototypical device design incorporates arrays of doped silicon microwires, with n-type wires comprising a photoanode which drives an oxygen-evolving reaction, and p-type wires comprising a photocathode to drive the hydrogen-evolving reaction. Both arrays are embedded in a proton-permeable, transparent membrane which acts as a barrier between the two reactions while facilitating transport of protons across the barrier. Currently, a main impediment to device efficiency is the voltage drop evident in the microwire-polymer-microwire system. This voltage drop can be mitigated by reducing the series resistance at each indicated trouble point. This study investigated reducing the resistivity of the n-type microwires that compose the photoanode of the system.

The silicon microwires investigated in this study showed a number of interesting properties. Most notably, their piezoresistive response under strain increased with increasing doping concentration, a characteristic in direct opposition to the behavior generally observed by bulk and top-down silicon structures. This indicates a fascinating piezoresistive response in bottom-up microwires. The n-type wires investigated in this study were split into three sets: A, B, and C, with doping concentrations of $(1.7 \pm 0.1) \times 10^{17} \text{ cm}^{-3}$, $(3.6 \pm 0.1) \times 10^{17} \text{ cm}^{-3}$, and $(6.8 \pm 0.8) \times 10^{20} \text{ cm}^{-3}$, respectively. Set A showed an average piezoresistive coefficient of $(-3 \pm 1) \times 10^{-11} \text{ Pa}^{-1}$, Set B $(-5 \pm 2) \times 10^{-11} \text{ Pa}^{-1}$, and Set C $(-16 \pm 5) \times 10^{-11} \text{ Pa}^{-1}$. The anomalous effect may be due in part to the different growth mechanism used to produce bottom-up wires. The wires are likely to be reasonably defect free and exhibit uniform crystalline structure when compared to top-down microwires especially, which has been postulated to increase carrier transport in the lattice. In order to investigate this anomalous behaviour, further studies should be performed on bottom-up structures in direct comparison to top-down structures, on the same length scale, at low and degenerate doping levels.

Following from these results, the Set B n-type microwires investigated could feasibly produce a 49% reduction in resistivity for a 3.1% applied bending strain. This would correspond to approximately a 1% reduction in overall system resistance, assuming junction resistance and polymer resistance remain unchanged; while the contribution of this study is dwarfed by the large junction resistance between the n-type microwires and the polymer, it serves as a proof of concept for using piezoresistivity to reduce resistivity of

the wires themselves, which may be of utility in the p-type microwire/polymer system as well. Harnessing the piezoresistive response of silicon microwires to tune the array resistivity is a valid method of reducing the overall system resistance within the artificial photosynthesis device and warrants further investigation. Future work will also seek to characterize the optoelectronic response of the strained silicon microwires to incident light.

Appendix A

Appendix

MATLAB code for dispersion relationship plot.

```
%Kronig Penney Dispersion Relationship
```

```
function kronigpenney(L)
```

```
% Physical constants
```

```
e=1.6*10e-19;
```

```
Emax=50*e;
```

```
h=1.055e-34;
```

```
m=9.11e-31;
```

```
% Barrier strength P
```

```
P = 2;
```

```
% Area of the potential barriers
A = ((h*h)*P)/(m*L);

% Energy range
E=linspace(0,Emax,1e5);

% Find alpha
alpha=sqrt(2*m*E)/h;

% Find Kronig-Penney fcn
kpfunc = cos(alpha*L) + (P)*sin(alpha*L)./(alpha*L);

% Solve for left hand side of equation to find kL
kL=acos(kpfunc);

% Plot
plot(kL,E/1.6e-19)
xlabel('kL')
ylabel('Energy (eV)')
title('Dispersion relation')
axis([0 3.14 0 14])
```

References

- [1] D. Bloom, “7 billion and counting,” *Science*, vol. 333, 2011.
- [2] WorldBank. (2013) Energy use (kg of oil equivalent per capita). [Online]. Available: <http://data.worldbank.org/indicator/EG.USE.PCAP.KG.OE/countries/1W?display=graph>
- [3] S. Solomon, G.-K. Plattner, R. Knutti, and P. Friedlingstein, “Irreversible climate change due to carbon dioxide emissions,” *Proceedings of the national academy of sciences*, vol. 106, no. 6, pp. 1704–1709, 2009.
- [4] T. A. Boden, G. Marland, and R. J. Andres. (2010) Global, regional, and national fossil-fuel CO₂ emissions. [Online]. Available: 10.331/CDIAC/00001-V2010
- [5] V. Fedorov, “Interannual variability of the solar constant,” *Solar System Research*, vol. 46, no. 2, pp. 170–176, 2012.
- [6] R. B. Gupta, *Hydrogen Fuel: Production, Transport and Storage*, 1st ed. CRC Press, 2008.

- [7] M. A. Green, “The path to 25% silicon solar cell efficiency: history of silicon cell evolution,” *Progress in Photovoltaics: Research and Applications*, vol. 17, no. 3, pp. 183–189, 2009.
- [8] M. A. Green, K. Emery, Y. Hishikawa, W. Warta, and E. D. Dunlop, “Solar cell efficiency tables (version 44),” *Progress in Photovoltaics: Research and Applications*, vol. 22, no. 7, pp. 701–710, 2014.
- [9] R. Tidball, J. Bluestein, N. Rodriguez, and S. Knoke, “Cost and performance assumptions for modeling electricity generation technologies,” *Contract*, vol. 303, pp. 275–300, 2010.
- [10] G. Masson, M. Latour, M. Rekinge, I.-T. Theologitis, and M. Papoutsis. (2012) Global market outlook for photovoltaics 2013 - 2017. [Online]. Available: http://www.epia.org/fileadmin/user_upload/Publications/GMO_2013_-_Final_PDF.pdf
- [11] StatCanada. (2011) Table358-0214: Industrial energy research and development expenditures and extramural payments outside canada, by area of technology, annual (dollars). [Online]. Available: <http://www5.statcan.gc.ca/cansim/pick-choisir?lang=eng&p2=33&id=3580214>
- [12] H. Gray, “Powering the planet with solar fuel,” *Nature Chemistry*, vol. 1.
- [13] M. Walter, E. L. Warren, J. R. McKone, S. W. Boettcher, Q. Mi, E. A. Santori, and N. S. Lewis, “Solar water splitting cells,” *Chem. Rev.*, vol. 110, 2010.

- [14] EnerData. (2010) Average electricity consumption per electrified household. [Online]. Available: <http://www.wec-indicators.enerdata.eu/household-electricity-use.html>
- [15] D. H. Program. (2006) Hydrogen fuel cells fact sheet. [Online]. Available: http://www.hydrogen.energy.gov/pdfs/doe_fuelcell_factsheet.pdf
- [16] F. C. Strong, “Faraday’s laws in one equation,” *Journal of Chemical Education*, vol. 38, no. 2, p. 98, 1961.
- [17] I. Yahyaie, S. Ardo, D. R. Oliver, D. J. Thomson, M. S. Freund, and N. S. Lewis, “Comparison between the electrical junction properties of h-terminated and methyl-terminated individual si microwire/polymer assemblies for photoelectrochemical fuel production,” *Energy Environment Science*, vol. 5, 2012.
- [18] C. S. Smith, “Piezoresistance effect in germanium and silicon,” *Phys. Rev. Lett.*, vol. 94, pp. 42 – 49, 1954.
- [19] R. He and P. Yang, “Giant piezoresistance in silicon nanowires,” *Nature Nanotechnology*, vol. 1, pp. 42 – 46, 2006.
- [20] J. Milne and A. Rowe, “Giant piezoresistance effects in silicon nanowires and microwires,” *Phys. Rev. Lett.*, vol. 105, p. 226802, 2010.
- [21] J. Feng, X. Qian, C. Huang, and J. Li, “Strain-engineered artificial atom as a broad-spectrum solar energy funnel,” *Nature Photonics*, vol. 6, no. 12, pp. 866–812, 2012.

-
- [22] J. Greil, S. Birner, E. Bertagnolli, and A. Lugstein, “Nanowires enabling strained photovoltaics,” *Applied Physics Letters*, vol. 104, no. 16, p. 163901, 2014.
- [23] Y. Kanda, “Piezoresistance effect of silicon,” *Sensors and Actuators*, vol. 28, pp. 83 – 91, 1991.
- [24] T. M. Adams and R. Layton, *Introductory MEMS: Fabrication and Applications*. New York: Springer, 2010.
- [25] M. Hopcroft, W. Nix, and T. Kennedy, “What is the young’s modulus of silicon?” *Journal of Microelectromechanical Systems*, vol. 19(2), p. 229, 2010.
- [26] K. Najafi and K. Suzuki, “Measurement of fracture stress, young’s modulus, and intrinsic stress of heavily boron-doped silicon microstructures,” *Thin Solid Films*, vol. 181, no. 1, pp. 251–258, 1989.
- [27] M. J. Madou, *Fundamentals of Microfabrication: The Science of Miniaturization*, 2nd ed. CRC Press, 2002.
- [28] F. Geyling and J. Forst, “Semiconductor strain transducers,” *The Bell System Technical Journal*, vol. 39, pp. 705 – 731, 1960.
- [29] J. C. Wolfe, “Summary of the kronig-penney electron,” *American Journal of Physics*, vol. 46, pp. 1012–1014, 1978.
- [30] A. Rowe, “Piezoresistance in silicon and its nanostructures,” *J. Mater. Res.*, vol. 29 (6), p. 731, 2014.

-
- [31] N. Mark. (2007) Condensed matter physics, lecture 7. [Online]. Available: <http://www.physics.usyd.edu.au/~nigel/phys3012/Lecture7-Normal.pdf>
- [32] R. Hoffman, “Solids and surfaces: A chemist’s view of bonding in extended structures,” *Cornell University, Baker Lab*, p. 271, 1988.
- [33] R. L. Sproull and W. A. Phillips, *Modern Physics: The Quantum Physics of Atoms, Solids and Nuclei*. John Wiley and Sons, 1980.
- [34] L. Solymar and D. Walsh, *Electrical Properties of Materials*, 8th ed. Oxford University Press, 2010.
- [35] C. Kittel, *Elementary Solid State Physics: A Short Course*. John Wiley and Sons, Inc, 1962.
- [36] S. O. Kasap, *Principles of Electronic Materials and Devices*, 3rd ed. McGraw-Hill, 2006.
- [37] C. Herring and E. Vogt, “Transport and deformation-potential theory for many-valley semiconductors with anisotropic scattering,” *Phys. Rev.*, vol. 101 (3), p. 944, 1956.
- [38] J. Bradby and J. Williams, “In situ electrical characterization of phase transformations in si during indentation,” *Physical Review B*, vol. 67, p. 085205, 2003.
- [39] R. Hull, *Properties of Crystalline Silicon*, 1st ed. IET, 1999.

-
- [40] J. Hu, L. Merkle, C. Menoni, and I. L. Spain, “Crystal data for high-pressure phases of silicon,” *Physical Review B*, vol. 34 (7), p. 4679, 1986.
- [41] F. Beer, E. R. Johnston, and J. T. DeWolf, *Mechanics of Materials*, 3rd ed. McGraw Hill, 2002.
- [42] K. Matsuda, K. Suzuki, K. Yamamura, and Y. Kanda, “Nonlinear piezoresistance effects in silicon,” *Journal of applied physics*, vol. 73, no. 4, pp. 1838–1847, 1993.
- [43] C. Dietrich, M. Lange, F. Klüpfel, H. Von Wenckstern, R. Schmidt-Grund, and M. Grundmann, “Strain distribution in bent zno microwires,” *Applied Physics Letters*, vol. 98, no. 3, p. 031105, 2011.
- [44] S. A. Campbell, *Fabrication Engineering at the Micro- and Nano-scale*. Oxford University Press, 2013.
- [45] P. Alpuim, J. Gaspar, and et al, “Study of the piezoresistivity of doped nanocrystalline silicon thin films,” *Journal of Applied Physics*, vol. 109, p. 123717, 2011.
- [46] Y. Kanda, “A graphical representation of the piezoresistance coefficients in silicon,” *IEEE Transactions on Electron Devices*, vol. 29, p. 64, 1982.
- [47] J. Kinoshita, “Piezoresistance and piezo-hall-effect in highly-doped n-type silicon,” *Journal of the Physical Society of Japan*, vol. 33 (3), p. 743, 1972.
- [48] O. Tufte and E. Stelzer, “Piezoresistive properties of heavily doped n-type silicon,” *Physical Review*, vol. 6A, p. 1705, 1964.

- [49] H. D. Tong, S. Chen, W. G. van der Wiel, E. T. Carlen, and A. van den Berg, “Novel top-down wafer-scale fabrication of single crystal silicon nanowires,” *Nano letters*, vol. 9, no. 3, pp. 1015–1022, 2009.
- [50] F. Li, P. D. Nellist, and D. J. Cockayne, “Doping-dependent nanofaceting on silicon nanowire surfaces,” *Applied Physics Letters*, vol. 94, no. 26, pp. 263 111–263 111, 2009.
- [51] F. Oehler, P. Gentile, T. Baron, P. Ferret, M. D. Hertog, and J. Rouviere, “The importance of radial growth in the faceting of silicon nanowires,” *Nanoletters*, vol. 10, p. 2335, 2010.
- [52] G. Stan, S. Krylyuk, A. Davydov, I. Levin, and R. Cook, “Ultimate bending strength of si nanowires,” *Nano letters*, vol. 12, no. 5, pp. 2599–2604, 2012.
- [53] A. Lugstein, M. Steinmair, A. Steiger, H. Kosina, and E. Bertagnolli, “Anomalous piezoresistance effect in ultrastrained silicon nanowires,” *Nanoletters*, vol. 10 (8), p. 3204, 2010.
- [54] E. Nemanick, P. Hurley, and B. Brunshwig, “Chemical and electrical passivation of silicon (111) surfaces through functionalization with sterically hindered alkyl groups,” *Journal of Physical Chemistry*, vol. 110 (30), p. 14800, 2006.
- [55] K. T. Wong and N. S. Lewis, “What a difference a bond makes: The structural, chemical, and physical properties of methyl-terminated si (111) surfaces,” *Accounts of chemical research*, 2014.

- [56] B. M. Kayes, “Growth of vertically aligned si wire arrays over large areas with au and cu catalysts,” *Applied Physics Letters*, vol. 91, p. 103110, 2007.
- [57] S. Boettcher and J. M. S. et al, “Energy-conversion properties of vapour-liquid-solid-grown silicon wire-array photocathodes,” *Science*, 2010.
- [58] S. Ruffell, J. E. Bradby, N. Fujisawa, and J. Williams, “Identification of nanoindentation-induced phase changes in silicon by in-situ electrical characterization,” *Journal of Applied Physics*, vol. 101, p. 083531, 2007.
- [59] A. Warren, A. Nylund, and I. Olefjord, “Oxidation of tungsten and tungsten carbide in dry and humid atmospheres,” *Int. J. of Refractory Metals and Hard Materials*, vol. 14, p. 345, 1996.
- [60] I. Yahyaie, K. McEleney, M. Walter, D. R. Oliver, D. J. Thomson, M. S. Freund, and N. S. Lewis, “Electrical characterization of si microwires and of si microwire/conducting polymer composite junctions,” *The Journal of Physical Chemistry Letters*, vol. 2, pp. 675–680, 2011.
- [61] W. Chen, L. Yu, S. Misra, Z. Fan, P. Pareige, G. Patriarche, S. Bouchoule, and P. R. i Cabarrocas, “Incorporation and redistribution of impurities into silicon nanowires during metal-particle-assisted growth,” *Nature communications*, vol. 5, 2014.
- [62] O. Moutanabbir, D. Isheim, H. Blumtritt, S. Senz, E. Pippel, and D. N. Seidman, “Colossal injection of catalyst atoms into silicon nanowires,” *Nature*, vol. 496, no. 7443, pp. 78–82, 2013.

-
- [63] A. Tavendale and S. Pearton, “Deep level, quenched-in defects in silicon doped with gold, silver, iron, copper or nickel,” *Journal of Physics C: Solid State Physics*, vol. 16, no. 9, p. 1665, 1983.
- [64] I. Yahyaie, K. McEleney, M. G. Walter, D. R. Oliver, D. J. Thomson, M. S. Freund, and N. S. Lewis, “Characterization of the electrical properties of individual p-si microwire/polymer/n-si microwire assemblies,” *The Journal of Physical Chemistry C*, vol. 115, no. 50, pp. 24 945–24 950, 2011.